Title:

Development of a Portable Multimetric Sensing System for Bridge Load Testing and Load-Carrying Capacity Evaluation

Author Information

Author names:

Junyoung Park[a], Junsik Shin[b] and Jongbin Won[c,*]

Affiliations:

[a]*Universal Design & Novel Solution (UDNS) Co., Ltd., Seongnam, 13558, Republic of Korea; pjy5451@gmail.com*

[b]*Department of Civil and Environmental Engineering, Chung-Ang University, Dongjak, Seoul, 06974, Republic of Korea; jacoom1030@cau.ac.kr*

[c]*Department of Structural Engineering Research, Korea Institute of Civil Engineering and Building Technology, Goyang, 10223, Republic of Korea; jbwon90@kict.re.kr*

Corresponding author:

**Corresponding author: Jongbin Won, Tel: +82-10-4312-4315, E-mail address: jbwon90@kict.re.kr*

Manuscript WITHOUT Author details Click here to view linked References

Abstract

Bridge load-carrying capacity evaluation relies on static and dynamic load tests measuring strain, displacement, and vibration. Conventional wired instrumentation is accurate but bulky and time-consuming to deploy, limiting field efficiency and on-site sensor verification. This study presents a portable, low-power multimetric measurement system that acquires three-axis acceleration and four-channel strain and estimates displacement offline through strain-based modal reconstruction with acceleration-derived frequency-domain scaling. The module integrates a 24-bit ADC, MEMS accelerometer, real-time clock, microSD storage, and Bluetooth Classic (SPP) communication, and its firmware performs synchronized acquisition at 1000 Hz with filtering and downsampling. A smartphone application starts each node, displays signals in real time, and aligns clocks without a base station. In laboratory tests, acceleration noise was 0.47–1.55 mg across three axes, strain noise was 0.69 με, and trigger offsets among simultaneously controlled nodes were within 0.05 s. Field validation was performed on an in-service steel box-girder bridge using a 25.34-t dump truck for static load cases and dynamic passes at 10–70 km/h. The offline displacement estimates agreed with a co-located linear variable differential transformer, with a maximum absolute peak error of 0.073 mm for the three static load cases and a correlation coefficient of 0.978 and a mean absolute error of 0.055 mm for a dynamic passage. These results indicate that the portable module can provide the responses required for load testing of steel-girder bridges without a cabled data logger, a base-station computer, or a fixed-reference displacement transducer.

Keywords: Bridge load testing; Load-carrying capacity; Multimetric sensing; Wireless sensor node; Low-power sensing; Displacement estimation

1. Introduction

Reliable measurement of bridge responses during load testing is essential for evaluating load-carrying capacity and structural performance and extending the service life of aging infrastructure subjected to increasing traffic demands [1, 2]. As bridges deteriorate over time, changes in stiffness and load distribution may lead to serviceability or safety concerns [3]. To verify the structural performance of existing bridges, static and dynamic load tests using test vehicles are commonly conducted, during which strain, displacement, and vibration responses are measured and compared with design expectations [4].

Static load tests aim to evaluate the bridge response under predefined loading conditions by measuring strain and displacement at critical sections, whereas dynamic load tests assess the amplification of structural response caused by vehicle motion at different speeds [5, 6]. Together, these tests provide essential information for evaluating serviceability performance, identifying stiffness changes, and confirming that the bridge response remains within acceptable limits specified in design and evaluation guidelines [7].

Conventional bridge load testing has primarily relied on wired measurement systems, in which strain gauges, accelerometers, and displacement sensors are connected to centralized data loggers or computers. Although such systems provide high measurement accuracy, they are bulky, require extensive cabling, and involve long installation and setup times [8-11]. Moreover, long lead wires are susceptible to noise, signal drift, and damage during field deployment, making repeated or routine load testing inefficient and labor-intensive [12-14]. Such inefficiencies hinder the accumulation of high-quality data essential for advancing infrastructure maintenance automation and supporting the development of digital twins of civil structures [15-18].

Recent advances in wireless sensor networks and Internet-of-Things (IoT) technologies have enabled more flexible bridge monitoring solutions. Several wireless platforms have demonstrated the feasibility of distributed data acquisition for bridge testing [19-26]. However, most existing wireless systems still depend on base-station computers or gateway nodes for coordination and data synchronization [27]. In field load testing, sensors are often installed in confined or shielded environments such as box girders, where wireless communication may be unstable. As a result, reliable time synchronization across multiple nodes and simultaneous acquisition of heterogeneous sensor data remain challenging. In addition, many wireless systems provide limited support for real-time data verification, making it difficult to detect faulty sensor attachment or poor signal quality during testing.

Contact-type displacement transducers such as LVDTs require a fixed reference beneath the bridge, which is often unavailable over roads or rivers [28, 29]. Reference-free alternatives using GNSS, radar, and fused acceleration and strain measurements have therefore been studied [30–35]. Among them, multimetric approaches that combine synchronized acceleration and strain measurements have been recognized as an effective means of estimating displacement [31, 32, 34, 35, 36]. Nevertheless, efficient field implementation remains limited by the scarcity of compact sensing systems capable of synchronized multimetric acquisition and on-site data quality verification [37–40]. Related wireless multimetric modules on the commercial Xnode platform have been reported by Won et al. [35] and Lawal et al. [39]. Those implementations rely on a gateway-oriented wireless platform for collection and control, whereas the present system uses a custom low-power node with mobile-phone triggering, on-site signal checking, and per-node time alignment without a gateway.

The practical bottlenecks in current bridge load testing can therefore be summarized as follows: (i) reliance on base-station computers, (ii) difficulty in achieving reliable time synchronization among distributed sensors, (iii) limited integration of multimetric sensing within a single device, and (iv) lack of real-time data quality assessment in the field. These limitations hinder efficient and repeatable load testing, particularly for in-service bridges.

This study develops a portable multimetric sensing system that addresses these bottlenecks. A mobile-phone application provides trigger-based operation, real-time response checking, and per-node time alignment without a base-station computer. Displacement responses are subsequently obtained offline from the synchronized acceleration and strain records, providing a practical alternative when reference-fixed displacement transducers are difficult to deploy.

Laboratory tests examine sensor noise in both the time and frequency domains and evaluate Bluetooth-based time synchronization under short-range conditions. Field validation is conducted on an in-service steel box-girder bridge to assess offline displacement estimation accuracy and structural responses under static and dynamic loading. The measured responses are further used to evaluate lateral load distribution, neutral-axis location, and impact-related metrics under explicitly stated modeling assumptions.

The remainder of this paper is organized as follows. Section 2 describes the sensing system and the offline displacement estimation procedure. Section 3 presents laboratory validation results, and Section 4 reports full-scale field validation under static and dynamic loading. Section 5 concludes the study.

2. Proposed Sensing System

This section describes the design and configuration of the proposed portable sensing system. The system was developed to replace conventional wired instrumentation with a compact, low-power, and easily deployable solution for bridge load testing. Fig. 1 illustrates the conceptual difference between the conventional method and the proposed approach. In traditional setups, strain gauges and displacement sensors such as LVDTs are connected to a data logger, computer, and external power supply through long cables. In contrast, the proposed system integrates all sensing and communication modules within a single unit and stores data on board while streaming real-time previews to a mobile device, which reduces cabling and field complexity.

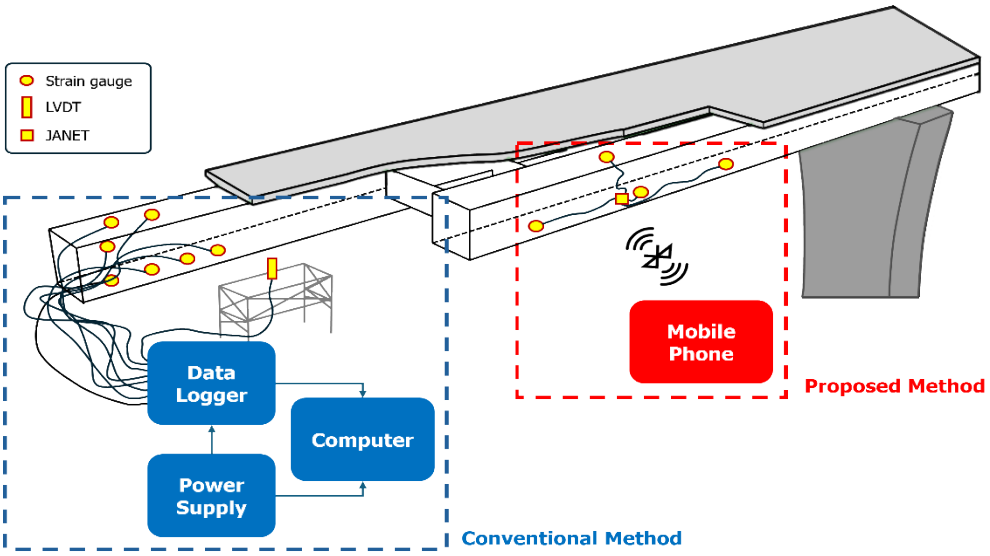


Fig. 1. Comparison between conventional and proposed methods

2.1. System Overview

The proposed system was developed to enhance the efficiency of bridge load-carrying capacity assessment by integrating multimetric sensing, synchronized data acquisition, and wireless communication into a single portable platform.

The hardware module consists of a microcontroller unit (MCU), a micro-electro-mechanical systems (MEMS) accelerometer for three-axis acceleration measurement, and a strain sensing circuit capable of acquiring four analog strain channels. The MCU controls sampling, local data storage, and Bluetooth-based wireless transmission, while a rechargeable battery supplies power for full-day field operation.

The software component includes embedded firmware that aligns the module clock with the phone reference time and manages data recording and transmission. A mobile application provides an interface for configuration, wireless control, and time synchronization.

2.2. Hardware Design

The hardware was developed as a compact and low-power sensing platform that integrates strain and acceleration measurements, data conversion, wireless communication, and local storage for efficient bridge load testing and load-carrying capacity assessment. Fig. 2 shows the printed circuit board (PCB) layout and external configuration of the sensor. The main components include an MCU, an analog-to-digital converter (ADC), a MEMS accelerometer, a real-time clock (RTC), a Bluetooth module, and a strain-sensing circuit.

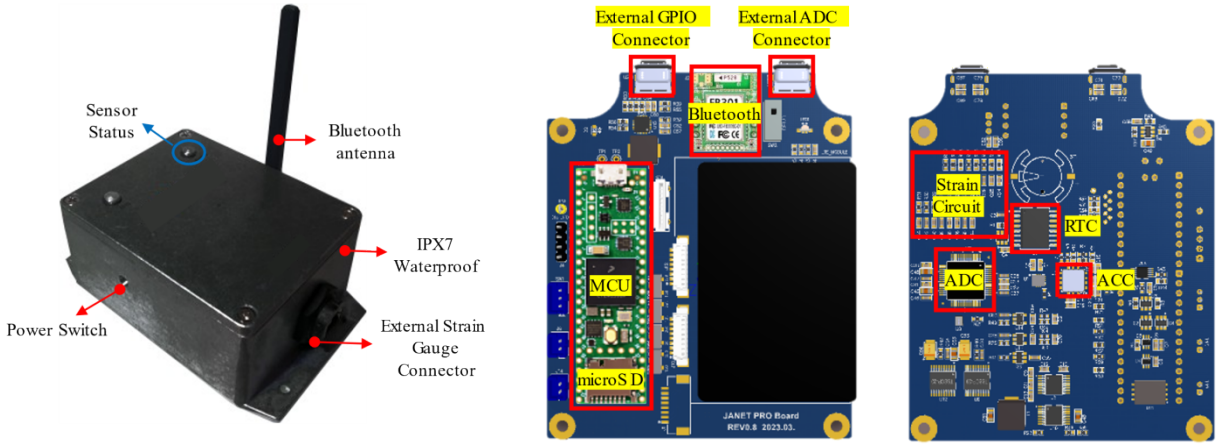


Fig. 2. Photograph and PCB layout of the developed sensor

The Teensy 4.1 (PJRC, USA) serves as the central processing unit for synchronized data acquisition and communication [41]. It controls sampling timing for strain and acceleration, manages on-board data logging, and relays commands and sensor data to the mobile application. Global time is referenced from the DS3231 RTC (1 s resolution), while millisecond timestamps are formed by combining the RTC second with an MCU sample counter. A built-in microSD slot enables autonomous local recording without a base-station computer, which improves field efficiency. The MCU communicates with the ADC and accelerometer through SPI, with the RTC through I²C, and with the Bluetooth module through UART.

The ADS131E08 (Texas Instruments, USA) is employed as an 8-channel, 24-bit delta-sigma ADC to digitize analog strain signals from the Wheatstone-bridge-based sensing circuit [42]. Four of the eight channels are used for strain in the present configuration. Each channel uses one active gauge with fixed completion resistors in a quarter-bridge arrangement without a dummy gauge for temperature compensation. The relationship between the differential voltage and the measured strain can be expressed as follows [43]:

$$\varepsilon = \frac{\Delta V \cdot 4}{GF \cdot V_{EXT}} \tag{1}$$

where ΔV represents the differential output voltage of the bridge, GF is the gauge factor of the strain gauge defined as $GF = (\Delta R/R)/\varepsilon$, R denotes the unstrained resistance, ΔR is the change in resistance caused by strain, and V_{EXT} represents the excitation voltage.

The ADXL355 (Analog Devices, USA) is adopted as a MEMS accelerometer that measures three-axis acceleration with low noise and high linearity, providing stable data for vibration analysis and displacement

estimation [44]. The device provides digitally converted acceleration data to the MCU and is used together with strain measurements during load testing.

The DS3231 (Maxim Integrated, USA) provides precise timekeeping for timestamping and inter-module consistency [45]. Timing information is retained during power cycles via a backup coin cell, supporting continuous logging workflows.

The FB755AS (Firmtech, South Korea) Bluetooth module provides short-range wireless communication between the MCU and a mobile device [46]. The module supports Bluetooth Classic communication using the Serial Port Profile (SPP) and interfaces with the MCU through UART. This configuration allows the sensor to transmit measured data and receive control commands without requiring a base-station computer.

Fig. 3 illustrates the power and interface architecture of the developed sensor. A rechargeable lithium-polymer battery supplies the module, and three independent voltage regulators distribute power to the analog sensing, digital processing, and wireless communication sections, respectively. This separation reduces electrical interference between the analog and digital circuits.

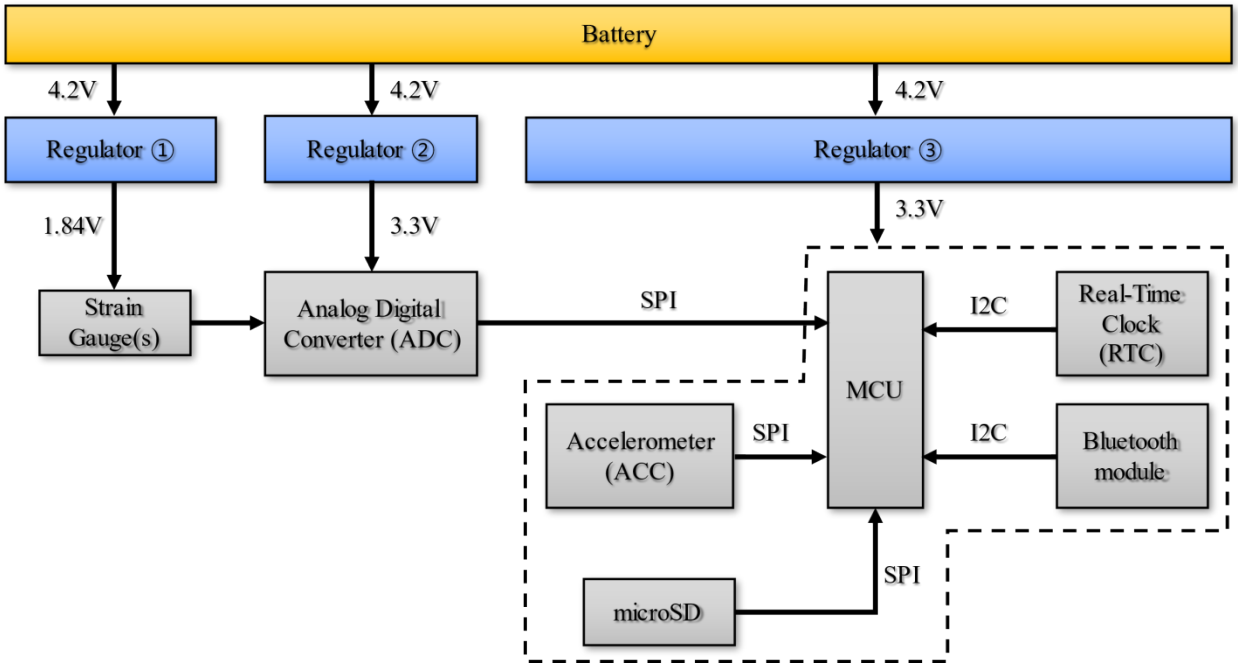


Fig. 3. Power and interface architecture of the developed sensor

2.3. Power Consumption Analysis

The power consumption of the developed sensor was estimated using the typical current values of each hardware component to evaluate the effectiveness of its low-power design. The total current consumption was obtained by summing the typical operating currents of major functional modules in the circuit.

Table 1 summarizes the representative current consumption of the main hardware modules. The MCU accounted for the largest portion of total current usage, followed by the power-regulation circuits, the Bluetooth module, the strain-gauge excitation, and the ADC. The accelerometer contributed minimally, and the RTC is omitted from Table 1 because its supply current is negligible [45]. The total estimated current draw of the developed sensor during active operation was approximately 235.2 mA [47].

A 10,500 mAh lithium-polymer battery was used as the power source. Based on this capacity, the theoretical continuous operating time T of the system can be calculated as:

$$T = \frac{C_{bat}}{I_{total}} = \frac{10500}{235.2} \approx 44.6\ h \tag{2}$$

where C_{bat} is the battery capacity (mAh) and I_{total} is the total current consumption (mA), which gives T in hours. This operating time is sufficient for typical bridge load testing campaigns, which generally require several hours of continuous data acquisition in the field. This estimate is based on typical datasheet currents and neglects battery derating.

Table 1. Summary of current consumption

Component	Function	Typical Current (mA)
MCU (Teensy 4.1)	Control and data acquisition	100
ADS131E08	Analog-to-digital conversion	16
ADXL355	Acceleration measurement	0.2
FB755AS	Wireless communication (SPP)	40
Power and regulation circuits	Voltage conversion and protection	59
Strain gauges (×4)	Bridge excitation	20
Total Consumption (active mode)		235.2

2.4. Software Development

2.4.1. Software Framework

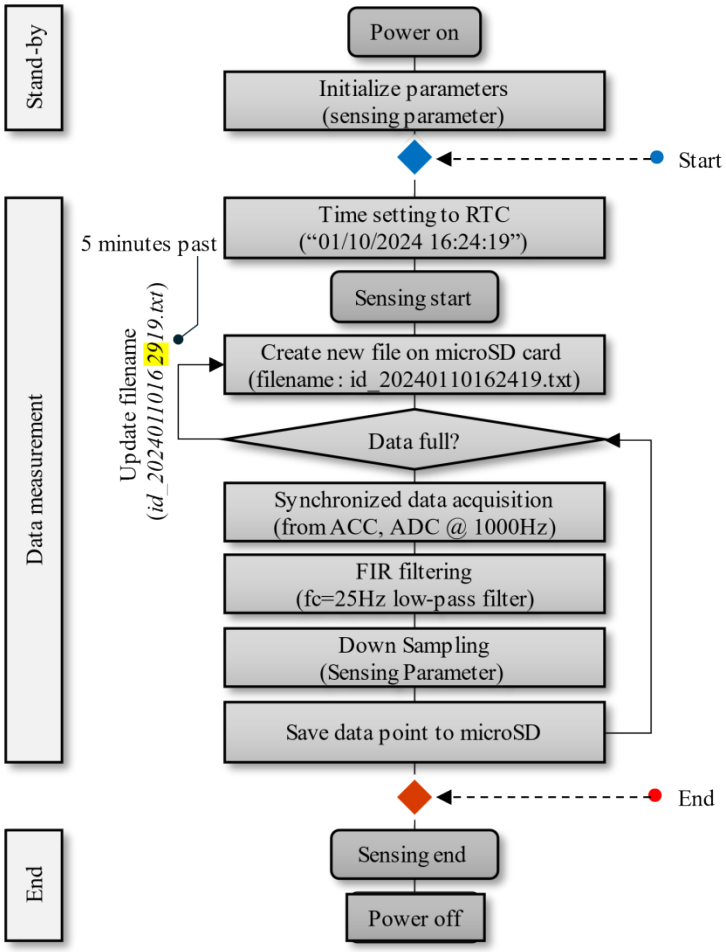


Fig. 4. Flowchart of the sensor software in continuous measurement mode

A software framework was developed to operate the sensing system. Fig. 4 presents the flowchart of this framework, which enables continuous measurement during bridge load testing. The operation consists of three sequential phases: (1) stand-by, (2) data measurement, and (3) end.

When the power switch is toggled, all parameters are initialized, including the file creation period, sampling frequency of the ADC and accelerometer, and Bluetooth identifier. The sensor enters a stand-by mode until it receives a trigger signal from the mobile application. This approach minimizes unnecessary power consumption and prevents premature data logging before testing begins.

Strain gauges typically experience drift when powered due to self-heating and excitation voltage instability, which diminishes after a warm-up period [48]. Hence, it is beneficial to power the sensor

immediately after sensor installation, even several hours before the load testing. Owing to its sufficient battery capacity, the sensor can remain powered for up to a day before the test.

When a trigger signal is received, the firmware synchronizes the embedded RTC with the transmitted reference time from the mobile application and begins recording. Data acquisition is performed at a predefined sampling frequency of 1000 Hz. Two general-purpose input/output (GPIO) interrupt pins are configured to synchronize sampling between the ADC and the accelerometer. At each sampling instance, both acceleration and strain signals are acquired when the interrupt signals indicate measurement completion (Fig. 5).

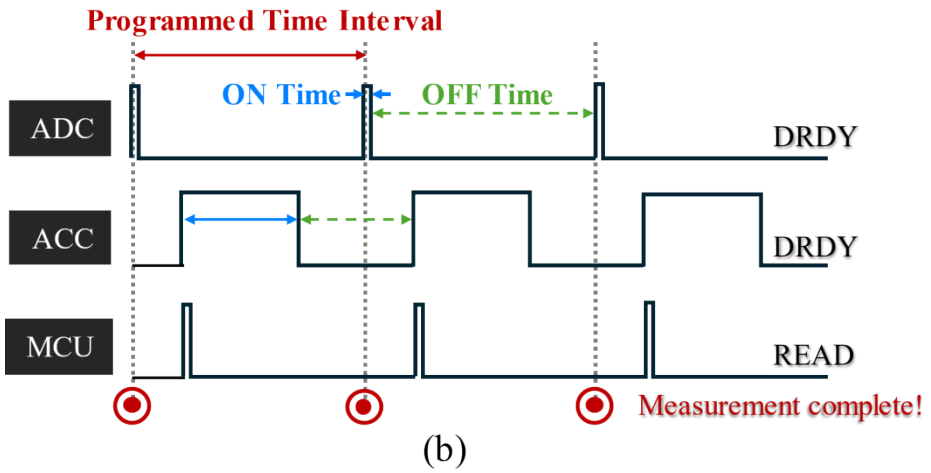


Fig. 5. Data acquisition timing diagram

2.4.2. Data Processing and Filtering

Once raw data are sampled at 1000 Hz, an on-board FIR low-pass filter with a cutoff frequency of 20 Hz and an order of 250 is applied, and the records are downsampled by a factor of 10 to 100 Hz for storage. Consequently, one data point comprising three-axis acceleration and four-channel strain is generated every 0.01 s. In post-processing, a fifth-order Butterworth low-pass filter with a 10 Hz cutoff was applied to the stored 100 Hz records.

Each data point is written to the active text file on the microSD card. To prevent individual text files from becoming excessively large, new files are automatically generated at predefined intervals (e.g., every 5 minutes). After all load testing is completed, the sensor can be powered off either by toggling the power switch or by issuing a stop command from the mobile application.

2.4.3. Mobile Application

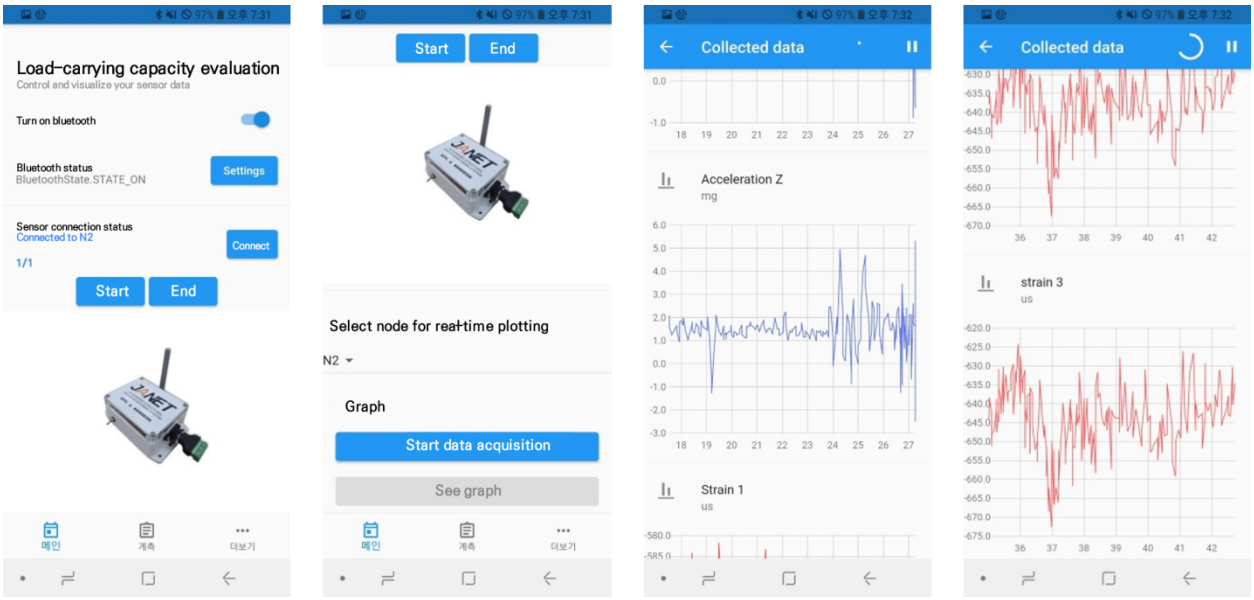


Fig. 6. Developed mobile application

The quality of acquired data can be easily degraded when a strain gauge is improperly attached, disconnected, or damaged during testing. In wired systems, such issues are typically identified through manual inspection on the DAQ or a connected computer, while real-time data verification is not supported in many wireless systems. To overcome these limitations, a mobile application was developed, enabling users to monitor sensor responses in real time and promptly identify potential measurement errors on-site.

The application was implemented using Flutter, an open-source cross-platform development framework by Google, and communicates with the sensor's built-in Bluetooth Classic at an update rate of 100 Hz. The app receives measurement data in real time and simultaneously visualizes dynamic responses such as strain and acceleration on a graphical interface. Fig. 6 shows the user interface of the mobile application, including device connection, measurement control, and real-time data visualization.

After launching, the application scans for nearby Bluetooth Classic devices and lists available sensor units. The operator may connect to a single node or to multiple nodes within range. In the intended field workflow, nodes are usually commissioned one by one after installation inside the girder: the phone sends a time reference, starts acquisition, and displays real-time strain and acceleration traces for on-site quality checking before the next node is configured. Simultaneous start of several connected nodes is available as an optional mode when wireless connectivity permits, but multi-node control from one phone is not a prerequisite for synchronized load testing.

This real-time feedback enables immediate verification of measurement quality on-site. If abnormal signals or unstable baselines are observed, operators can promptly identify the corresponding sensor and reattach or replace the faulty gauge before proceeding with the load testing. This reduces the risk of invalid records caused by unnoticed sensor faults.

In addition to real-time visualization, the application provides phone-based time alignment of each node's RTC. Because every node is visited during installation, time can be written locally when that node is started, which avoids reliance on a single phone simultaneously reaching all girders through the steel box. Each node then logs data autonomously until the test ends. The mobile-phone-based time synchronization and measurement-trigger concept is illustrated in Fig. 7.

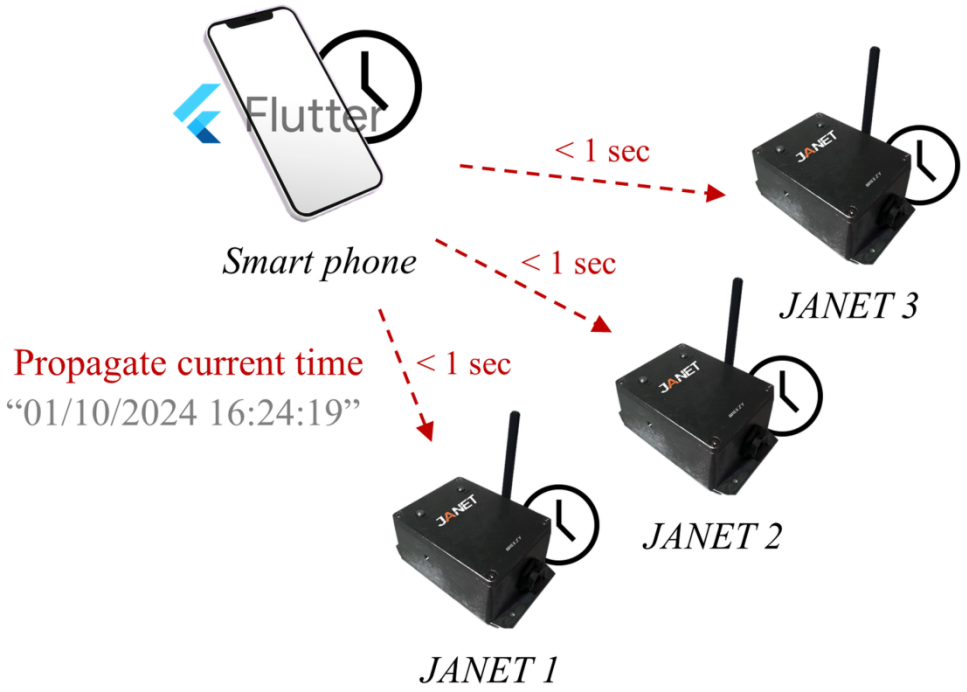


Fig. 7. Mobile-phone-based time synchronization and measurement trigger.

2.4.4. Indirect Displacement Estimation

Displacement is not measured directly. It is estimated offline from the stored strain and acceleration records by combining strain-based modal reconstruction with frequency-domain amplitude scaling derived from acceleration, without double integration of acceleration.

The objective of the indirect displacement estimation is to reconstruct the displacement response at a predefined target location. The displacement at this target location can be approximated using modal coordinates as:

$$u_x(t) = \Phi_x q(t), \tag{3}$$

where $u_x(t)$ is the displacement at the target location x, Φ_x is the displacement mode-shape row vector evaluated at the target location, and $q(t)$ is the modal coordinate vector. The strain responses measured at the strain-gauge locations can be related to the same modal coordinates as:

$$\varepsilon(t) = \Psi q(t), \tag{4}$$

where $\varepsilon(t)$ is the vector of measured strains and Ψ is the strain-related mode shape matrix at the strain gauge locations. In practice, Ψ includes the curvature-mode relationship up to constant scale terms associated with the neutral-axis distance, sign convention, and unit conversion. In this study, these constant scale terms were not used to directly determine the absolute displacement amplitude. Instead, the strain-based reconstruction was first used to obtain the relative displacement response history, and the absolute amplitude was calibrated using the acceleration-derived displacement spectrum.

For the field application in this study, the global bending response of the selected bridge span was approximated using an analytical sine mode shape based on a simply supported Euler–Bernoulli beam representation. For the j-th mode, the displacement mode-shape component at the target displacement location x is given by

$$\Phi_{x,j} = \sin(j\pi x/L), \tag{5}$$

where L is the span length. The corresponding strain-related mode shape component at the i-th strain gauge location $x_{\varepsilon,i}$ can be written in proportional form as:

$$\Psi_{ij} \propto j^2 \sin(j\pi x_{\varepsilon,i}/L), \tag{6}$$

where Ψ_{ij} is the strain-related mode shape component for the i-th strain gauge and the j-th mode. For a sine mode, the curvature term is proportional to $-(j\pi/L)^2 \sin\left(j\pi x_{\varepsilon,i}/L\right)$. In the implemented reconstruction, the constant scale terms, including $-(\pi/L)^2$, the neutral-axis distance, the strain unit conversion, and the sign convention, are absorbed into the subsequent frequency-domain scaling factor. Therefore, only the relative strain-mode shape was used to estimate the unscaled modal coordinate. This

analytical mode-shape representation was adopted as an engineering approximation of the global bending response of the selected span.

Using the measured strain vector, an unscaled modal coordinate vector can be estimated in a least-squares sense using the Moore–Penrose pseudo-inverse of the strain-related mode-shape matrix:

$$\tilde{q}(t) = \Psi^{\dagger}\varepsilon(t), \tag{7}$$

where $\Psi^{\dagger}$ is the Moore–Penrose pseudo-inverse of Ψ, and $\tilde{q}(t)$ denotes the unscaled modal coordinate estimate. The corresponding unscaled displacement response at the target location is then reconstructed as:

$$\tilde{u}s(t) = \Phi_x\tilde{q}(t). \tag{8}$$

In the field test, the strain gauges used for displacement reconstruction were installed at three longitudinal locations along the span, and the target displacement location was selected to correspond to the reference displacement measurement location. The first global bending mode was used for the reconstruction because the measured response was dominated by the first bending component in the frequency range of interest.

To determine the absolute displacement amplitude, the measured acceleration response was converted into an acceleration-derived displacement response using the regularized finite impulse response (FIR) filter proposed by Lee et al. [49]. This procedure was used to suppress low-frequency drift, which is unavoidable in direct double integration of acceleration. The acceleration-derived displacement response was not used as a direct estimate of static displacement. Instead, it was used as a spectral reference for calibrating the amplitude of the strain-based displacement estimate.

The frequency-domain scaling factor α was determined by comparing the power spectral densities of the acceleration-derived displacement response and the unscaled strain-derived displacement response in the dominant bending frequency band:

$$\alpha = \sqrt{\frac{S_{x_i}^{disp,\,acc}(f)}{S_{x_i}^{disp,\,strain}(f)}}, \tag{9}$$

where $S_{x_i}^{disp,\,acc}(f)$ and $S_{x_i}^{disp,\,strain}(f)$ denote the power spectral densities of the displacement estimated from acceleration and strain at location x_i, respectively, at the frequency f. In this study, the dominant bending frequency band was selected from preliminary vibration information and refined using

the acceleration PSD measured under ambient traffic excitation. The scaling factor was calibrated once using the ambient traffic response with fixed PSD parameters.

The final displacement estimate was obtained as:

$$\hat{u}(t) = \alpha \tilde{u}s(t). \tag{10}$$

For static load, acceleration was not used as a direct source of displacement because acceleration does not contain static displacement information. The static displacement response was obtained by applying the linear strain–modal mapping to the absolute strain records of each parked load case and scaling with the pre-calibrated factor α.

For dynamic passages, the same mapping and α were applied to the strain records referenced to the start of each passage, and no additional high-pass filtering or baseline correction was applied.

The present implementation does not require a detailed finite-element model, but it does rely on limited a priori geometric information, namely the span length, the longitudinal coordinates of the strain gauges, and the target displacement location.

Accordingly, the method is not automatically applicable to bridges without reliable prior modal information. For such structures, preliminary ambient modal identification, design- or inspection-based mode shapes, or temporary reference displacement calibration at one station is required before the estimator can be applied. The portable system can acquire the synchronized acceleration and strain data needed for preliminary characterization, but modal identification is outside the automated workflow demonstrated here.

Principal sources of uncertainty include mode-shape mismatch, strain-gauge bonding and positioning errors, temperature-induced apparent strain, low-frequency MEMS acceleration noise affecting spectral scaling, filter-parameter selection, and reference LVDT installation uncertainty. The complete offline estimation workflow is summarized in Fig. 8.

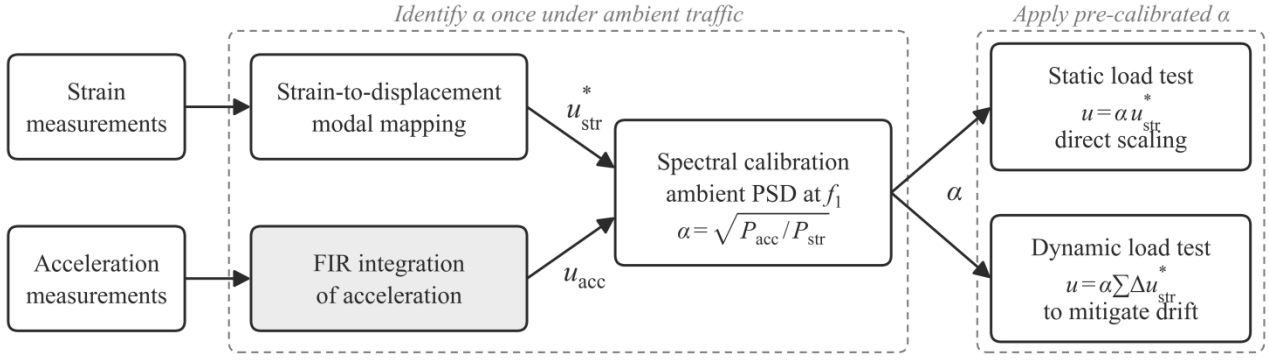


Fig. 8. Offline displacement estimation workflow.

3. Laboratory Scale Validation

This section presents laboratory-scale experiments conducted to validate the performance of the developed sensor system prior to field deployment. The experiments aim to (1) evaluate the signal quality of the integrated acceleration and strain measurement modules, and (2) evaluate the timing offsets of the optional simultaneous trigger among multiple sensor nodes.

3.1. Signal Noise Analysis

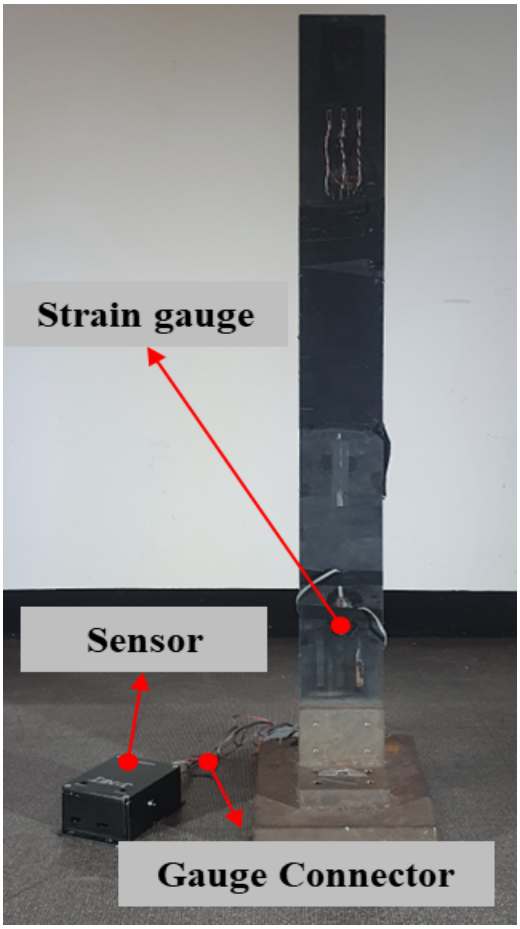
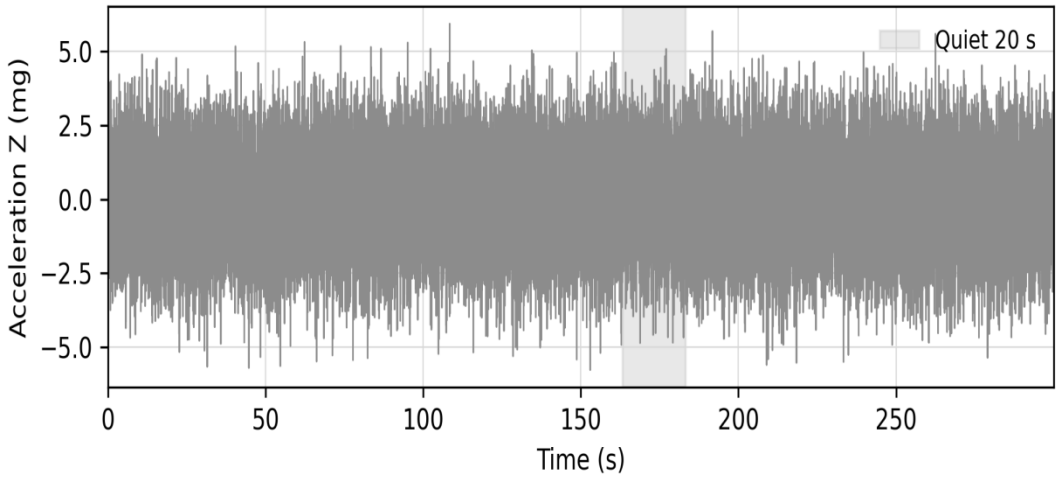


Fig. 9. Laboratory setup for sensor noise measurement.

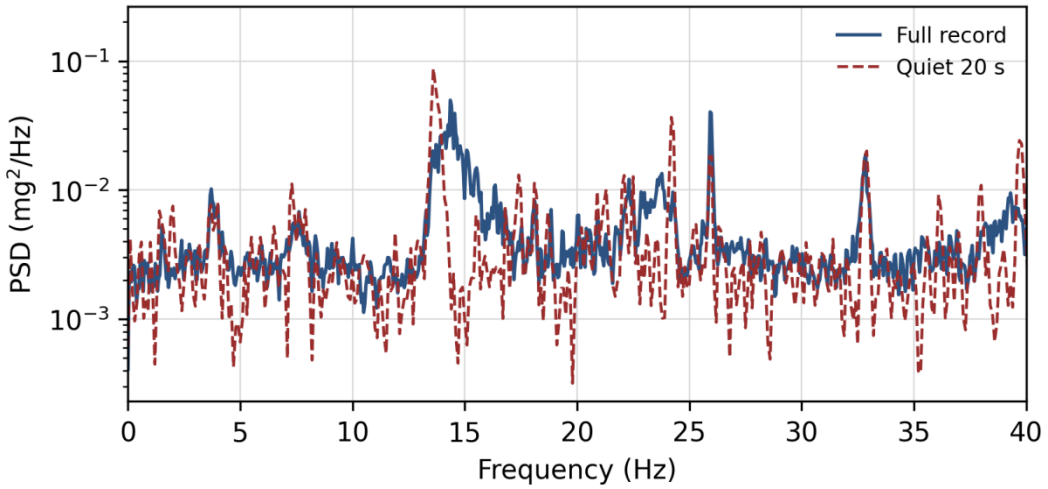
To assess the signal quality, noise measurements were performed using a laboratory-scale cantilever beam specimen with dimensions of 900 mm × 100 mm × 5 mm. A 350 Ω strain gauge (FLAB-5-350-11-3LJCT-F, Tokyo Measuring Instruments Laboratory Co., Ltd. [50]) with a gauge factor of 2.09 was attached

to the bottom surface of the beam, while the sensor unit was placed in a vibration-free environment to obtain representative noise levels under static conditions (Fig. 9).

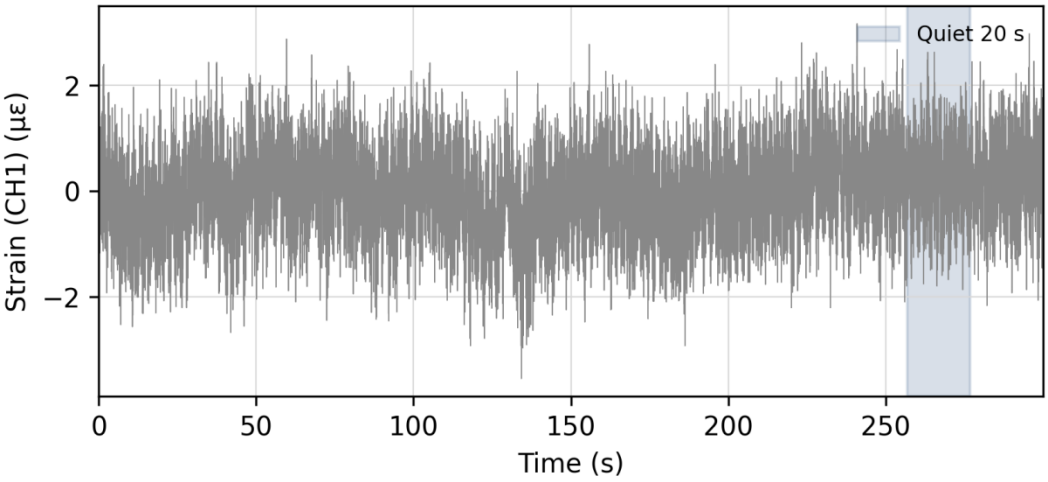
Acceleration and strain signals were recorded under laboratory quiet conditions at 100 Hz. Each quiet-lab record lasted approximately 300 s, from which the quietest 20 s window (lowest moving standard deviation) and 15 non-overlapping 20 s blocks were taken; Welch power spectral densities were computed on the full mean-removed (demeaned) record. The quiet-window spectrum is shown for comparison. The resulting time- and frequency-domain noise characteristics are shown in Fig. 10. For the analyzed record, the quiet-window standard deviations were 0.47 mg for the Y axis (transverse), 1.50 mg and 1.55 mg for the X and Z axes, respectively, and 0.69 με for strain. Variation of the 20 s standard deviation among successive blocks remained small (approximately 0.01–0.03 mg for acceleration and 0.03 με for strain). Because MEMS accelerometer noise increases toward low frequencies, the acceleration channel was not used to recover static displacement and was used only for spectral scaling and dynamic characterization. The strain noise of 0.69 με is below 2.5% of the peak static strains measured in the field (Section 4.4).



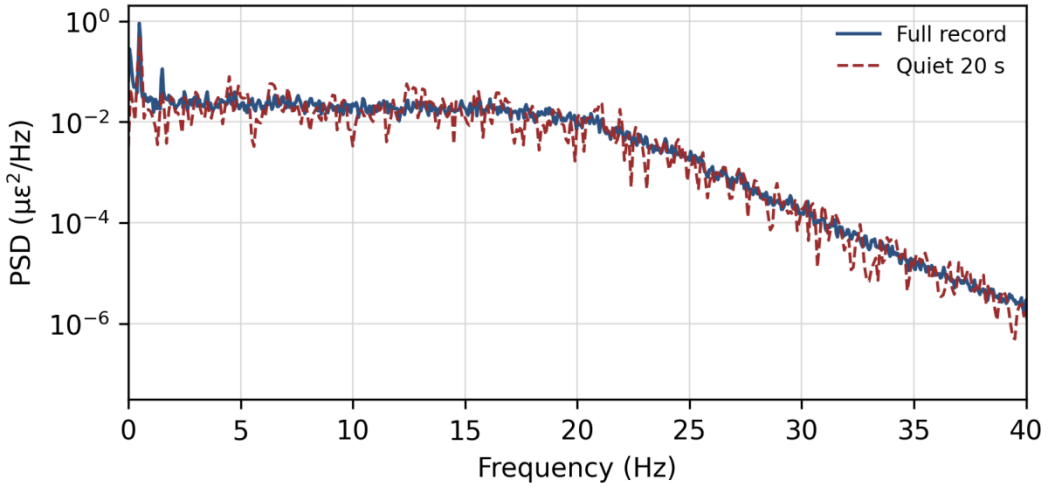
(a)


Full record
Quiet 20 s
PSD (mg²/Hz)
10⁻¹
10⁻²
10⁻³
0
5
10
15
20
25
30
35
40
Frequency (Hz)

(b)


Quiet 20 s
Strain (CH1) (με)
2
0
−2
0
50
100
150
200
250
Time (s)

(c)


Full record
Quiet 20 s
PSD (με²/Hz)
10⁰
10⁻²
10⁻⁴
10⁻⁶
0
5
10
15
20
25
30
35
40
Frequency (Hz)

(d)

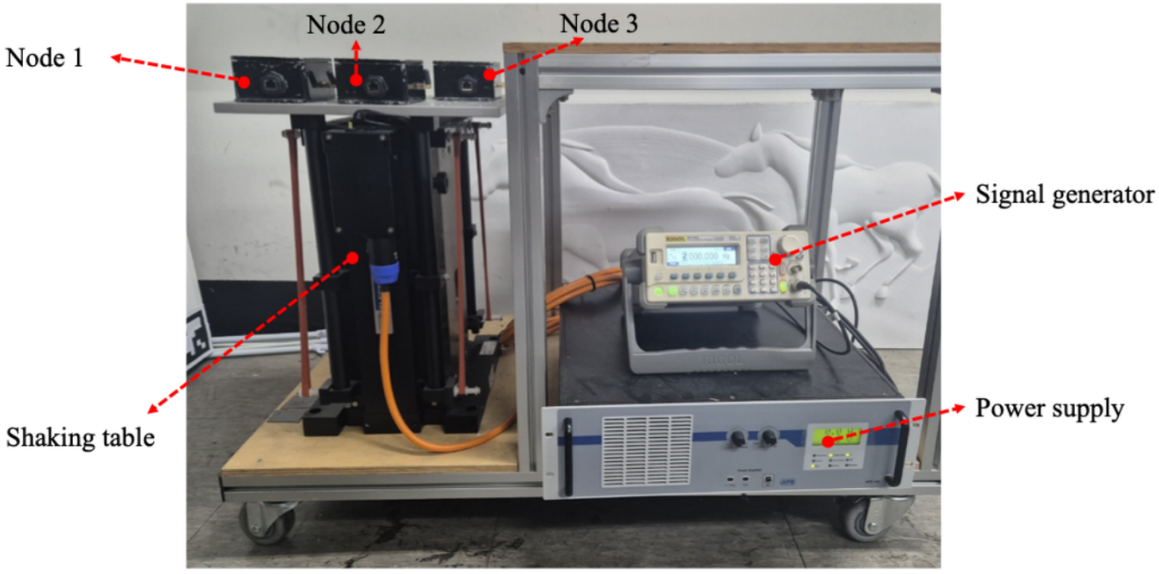
Fig. 10. Laboratory noise characterization: (a) vertical (Z) acceleration time history; (b) acceleration PSD; (c) strain time history; (d) strain PSD.

3.2. Time Synchronization using Bluetooth

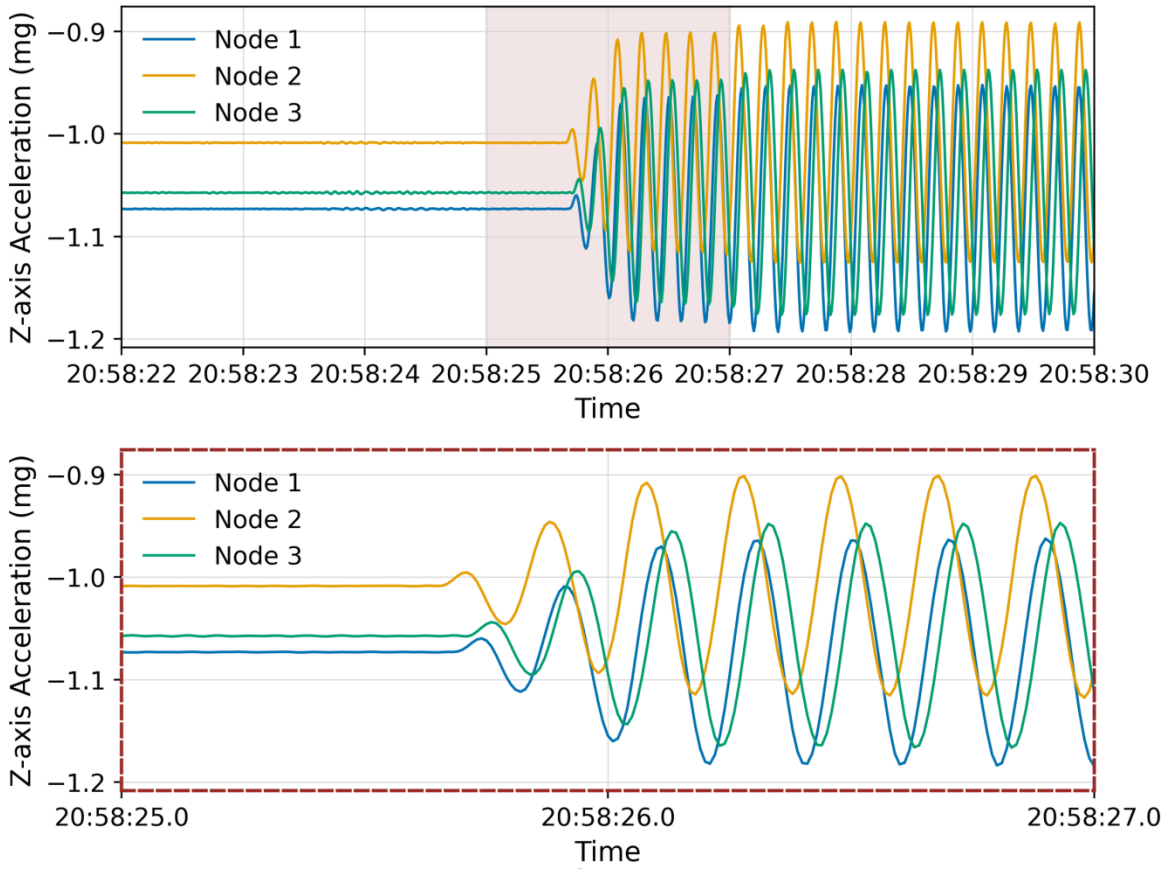
Accurate time synchronization across multiple sensor nodes is essential for conducting structural analysis using distributed measurements. To evaluate the optional simultaneous trigger, an experiment was conducted using three sensor units mounted on a shaking table, as shown in Fig. 11(a). From approximately 2 m away, the mobile application simultaneously propagated the global time reference and start command to each node via Bluetooth, after which the table was excited with a sinusoidal input.

Fig. 11(b) shows the superimposed acceleration responses collected from the three nodes. The timestamps of the first peak detected by Node 1, Node 2, and Node 3 were 20:58:25.710, 20:58:25.740, and 20:58:25.760, respectively. The resulting time differences relative to Node 1 were 0.03 s and 0.05 s, indicating timing offsets within 0.05 s at the 0.01 s resolution of the stored data. The offsets increased with node order, which suggests that sequential Bluetooth command latency may contribute to the offset.

Table 2 summarizes the laboratory synchronization results. This level of alignment is adequate for event alignment and peak-response comparison in load testing but not for phase-sensitive modal analysis. Simultaneous control was demonstrated only at a command distance of about 2 m.



(a)



(b)

Fig. 11. Time synchronization analysis: (a) experimental setup; (b) synchronized acceleration responses.

Table 2. Bluetooth-based time synchronization test results

Node name	1st peak global time	Difference
Node 1	20:58:25.710	-
Node 2	20:58:25.740	0.03 s
Node 3	20:58:25.760	0.05 s

4. Field Validation

This section presents the field validation of the developed sensor system through a full-scale load-carrying capacity evaluation conducted on the Bukbu Expressway in Seoul, Republic of Korea. The field tests were carried out to assess the system's performance under real bridge conditions, including multimetric sensing, indirect displacement estimation, load distribution assessment, and dynamic response analysis.

4.1. Validation Overview

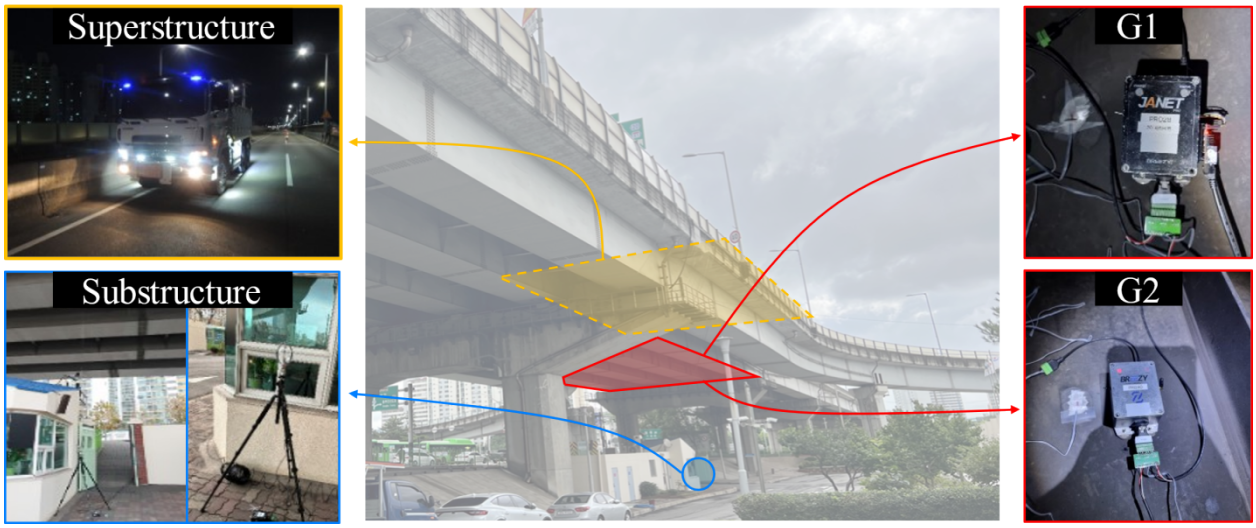


Fig. 12. Field validation on Bukbu Expressway, Seoul, Republic of Korea

The field validation was performed on November 15–16, 2023, on the Bukbu Expressway, a 6.6-km-long elevated urban expressway composed of steel box-girder spans connecting Guri and Jeongneung in Seoul (Fig. 12). The route carries an average daily traffic volume of 121,532 vehicles [51]. The BR-12 continuous unit (MP57–MP63; six spans) was selected for load testing. This region contains noticeable deterioration such as paint peeling, girder corrosion, and slab cracking, and features a longitudinally asymmetric configuration with mixed substructure types. Among the spans, the MP57–MP58 section was chosen as the primary test location because it corresponds to the maximum bending moment region and offers sufficient accessibility for sensor installation [52].

Two sensor nodes were installed on girders G1 and G2. Static tests used the test truck parked at three lateral positions (Static LC1–LC3) on section A–A, and dynamic tests comprised controlled passes at approximately 10–70 km/h in 10 km/h increments. The span length between bearings of MP57–MP58 is

47.14 m; the same length was used for displacement reconstruction and for the code impact-coefficient formula.

4.2. Experimental Setup

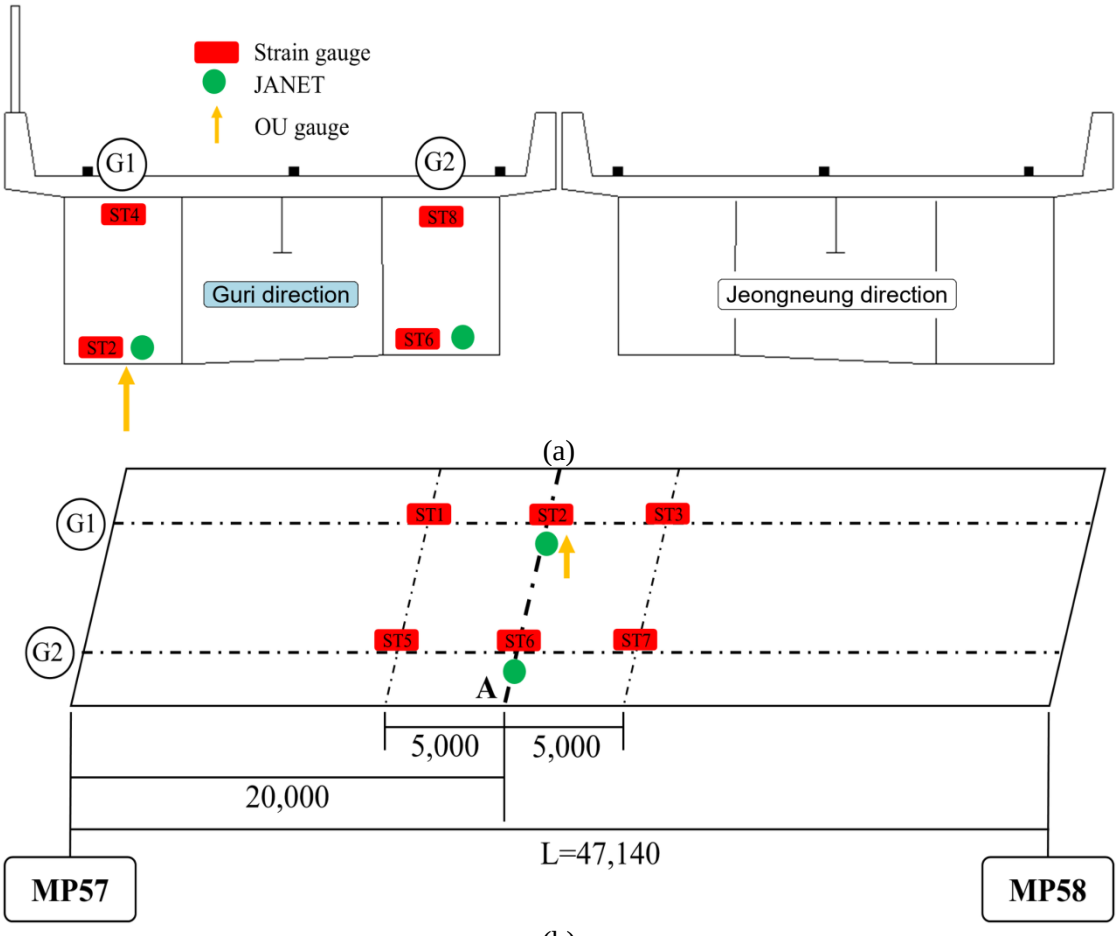


Fig. 13. Experimental setup: (a) section A–A; (b) sensor locations along the span (unit: mm).

Fig. 13 illustrates the deployment layout for the MP57–MP58 span, which consists of two steel box girders (G1 and G2). Two sensor units (J1 and J2) were installed on the bottom flange inside each girder (one unit per girder), approximately 20 m from one end of the span, corresponding to the maximum bending moment location.

A total of eight strain gauges (ST1–ST8) were installed along the bottom flange at −5 m, 0 m, and +5 m relative to each sensor node, with an additional gauge placed on the top flange at the 0 m location (i.e., 20 m) to support neutral axis estimation (Table 3).

For reference measurement, an LVDT was installed at the same location as sensor J1 on girder G1. A dump truck with a measured gross weight of 25.34 t was used for the loading tests, corresponding to 58.7% of the DB-24 design truck load (43.2 t) specified in the Korean Highway Bridge Design Code [53].

The vertical acceleration component (sensor Z axis) was used for displacement-related processing. Bottom-flange gauges at −5 m, 0 m, and +5 m relative to each node formed the multi-point strain vector for modal reconstruction, and the top-flange gauge at the node station supported neutral-axis estimation.

Representative raw strain records acquired during static loading are shown in Fig. 14.

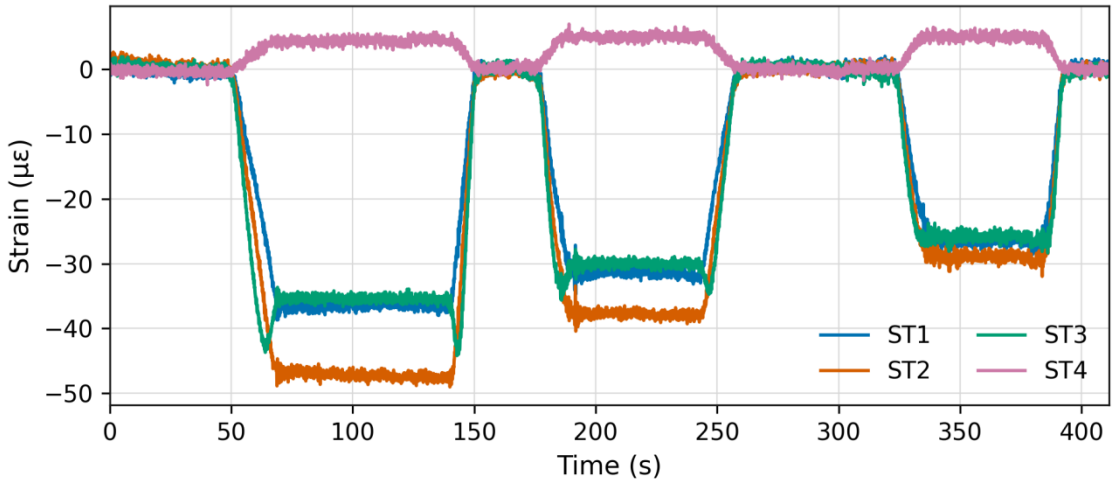


Fig. 14. Raw strain time histories at girder G1 under static loading (ST1–ST4).

Fig. 15 presents raw acceleration (Z) and four-channel strain (ST1–ST4) responses recorded during a dynamic truck passage. The test-truck configuration is shown in Fig. 16.

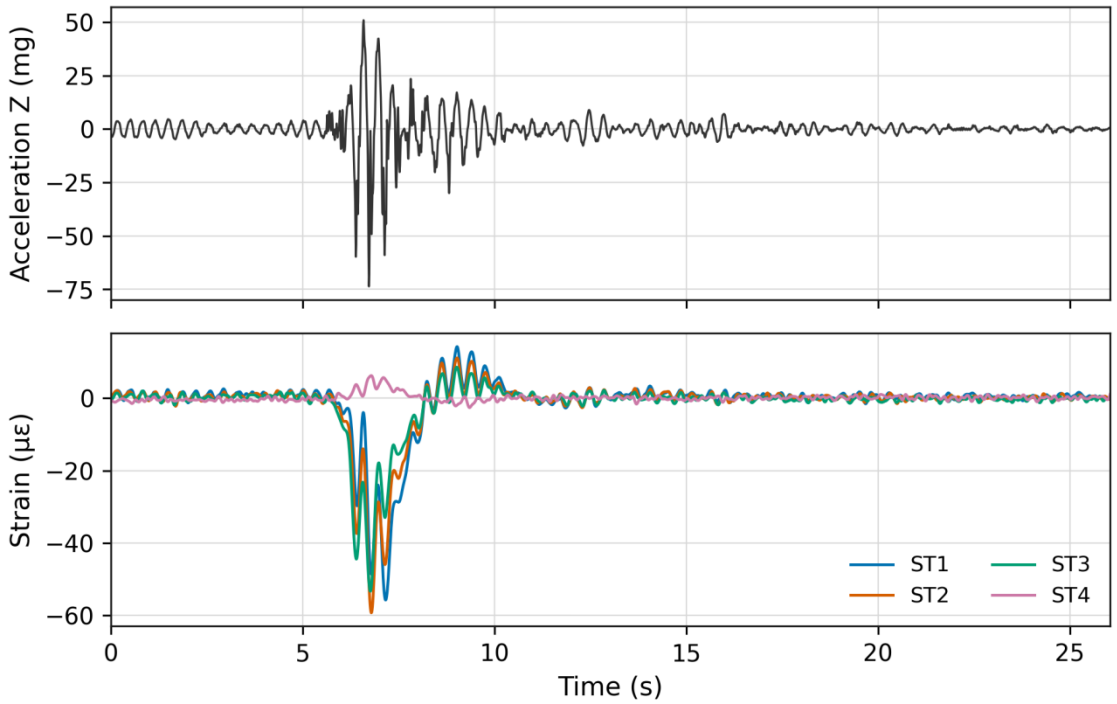


Fig. 15. Raw acceleration (Z) and strain (ST1–ST4) at the 20 m station of girder G1 during a dynamic truck passage.

Table 3. Summary of sensor types and locations

	Monitored Parameter	Position	Quantity
Proposed	Acceleration	J1–J2	2
	Strain	ST1–ST8	8
Reference	Displacement	J1	1

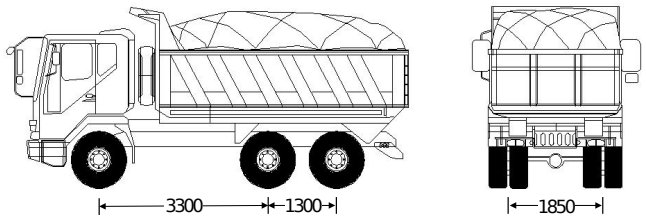


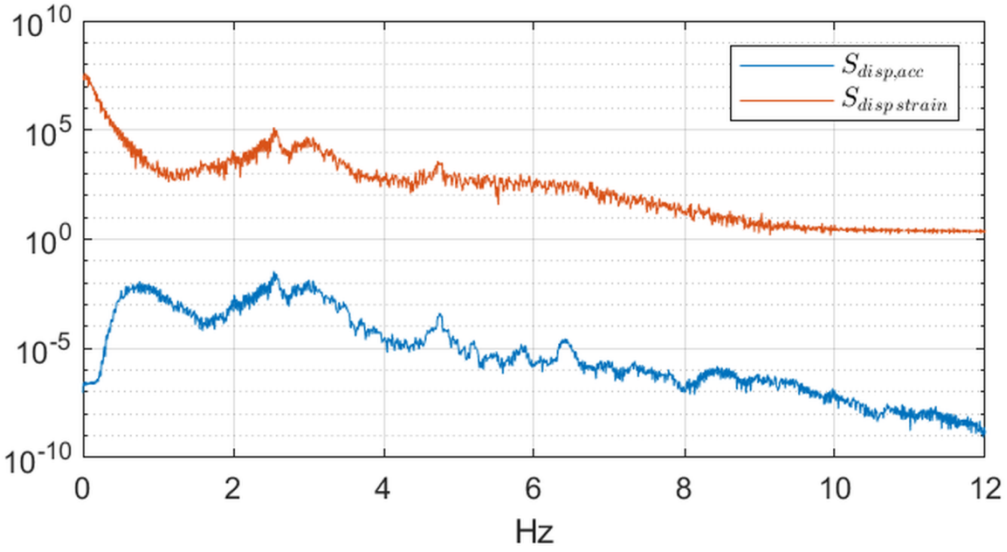
Fig. 16. Test truck specification

4.3. Calibration of Scaling Factor for Indirect Displacement Estimation

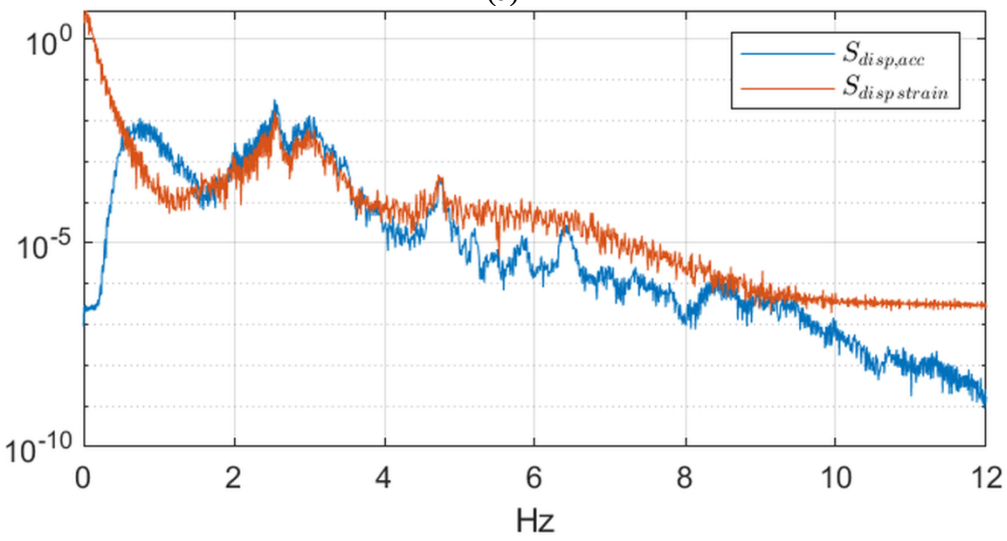
As described in Section 2.4.4, a frequency-domain scaling factor is required to match the spectral amplitudes of the acceleration- and strain-based displacement estimates. Ambient responses under normal traffic were recorded before the controlled truck tests and used to calibrate α independently for each girder using Eq. (9) in the 4–5 Hz band (G1: $\alpha = 2.72\times10^{-4}$; G2: $\alpha = 3.53\times10^{-4}$).

The reconstruction for G1 used L = 47.14 m, strain stations at 15, 20, and 25 m, and a single sine-mode approximation of the first bending shape. This simply supported mode was adopted as a simplified engineering approximation for the continuous side span. Fig. 17 shows the PSDs of displacement estimated from acceleration and strain at ST2. Both spectra exhibit a dominant peak at 4.77 Hz, corresponding to the first bending mode, with a lower peak at 2.54 Hz associated with torsion. The acceleration-derived displacement was obtained with the FIR filter described in Section 2.4.4, using a window length of 2.68 times the target period (Nw = 2.68) as recommended in [49].

Controlled static and dynamic truck responses were then compared with the co-located LVDT using records time-aligned by matching prominent response peaks. Peak errors for the three Static LC1–LC3 plateaus shown in Fig. 18 are summarized as the matched-static row in Table 4 (maximum absolute peak error 0.073 mm, MAE = 0.040 mm, RMSE = 0.046 mm). Over the full aligned static window spanning LC1–LC3, the correlation coefficient was R = 0.847 (MAE = 0.274 mm, RMSE = 0.573 mm). For an aligned dynamic truck passage (metrics computed over 100.5–134.8 s), R = 0.978, MAE = 0.055 mm, and RMSE = 0.083 mm (Table 4). In the dynamic passage, the largest error occurred around the main response peak (Fig. 19).



(a)



(b)

Fig. 17. PSD of displacement from acceleration and strain: (a) without scaling; (b) with scaling.

Time-history comparisons between the co-located LVDT and the proposed estimates under static loading are shown in Fig. 18.

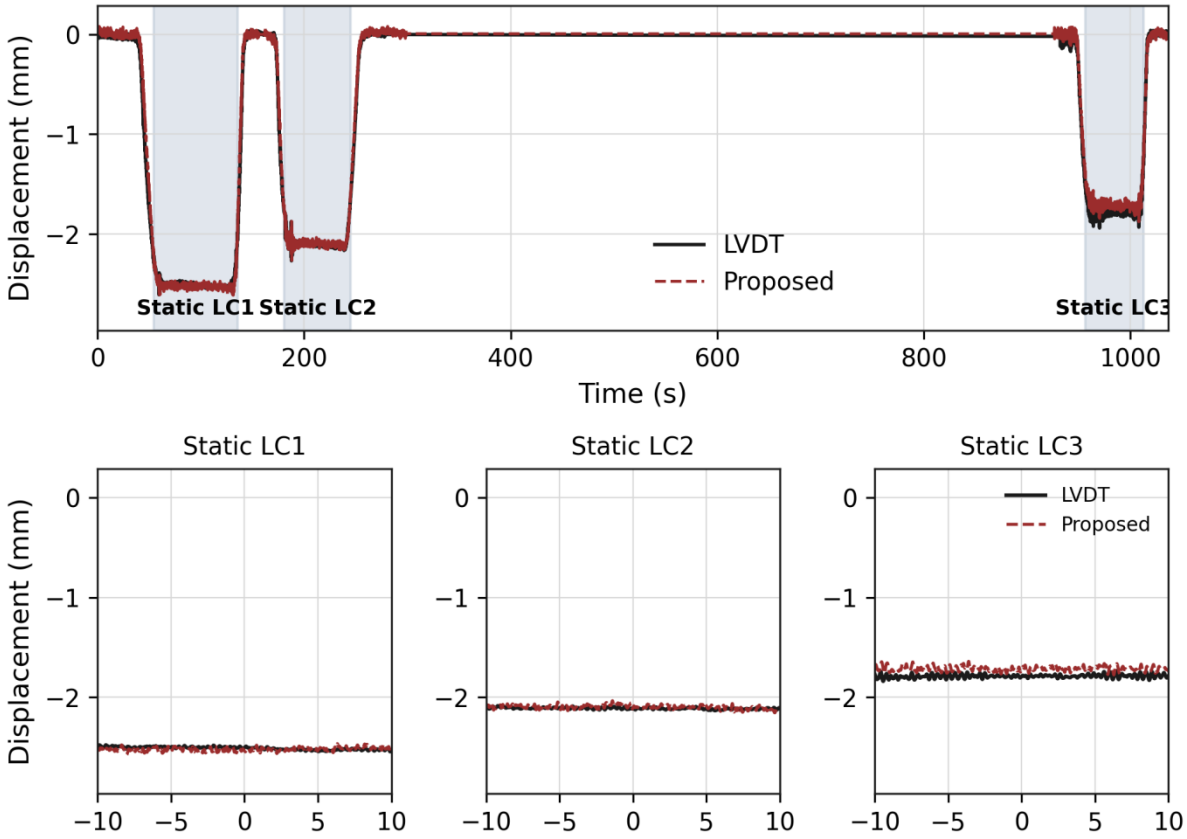


Fig. 18. Static displacement at G1: LVDT versus the proposed estimate for Static LC1–LC3.

An aligned dynamic passage is compared in Fig. 19. Quantitative metrics for this comparison are reported in Table 4 (computed over 100.5–134.8 s).

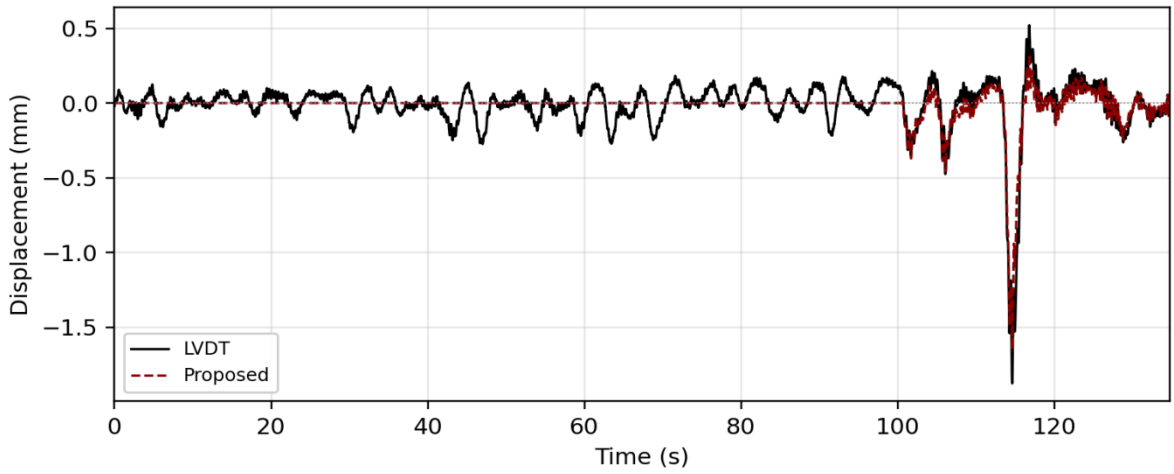


Fig. 19. Dynamic displacement at G1: LVDT versus the proposed estimate.

Fig. 20 compares the peak displacements from the LVDT and the proposed method for the matched Static LC events.

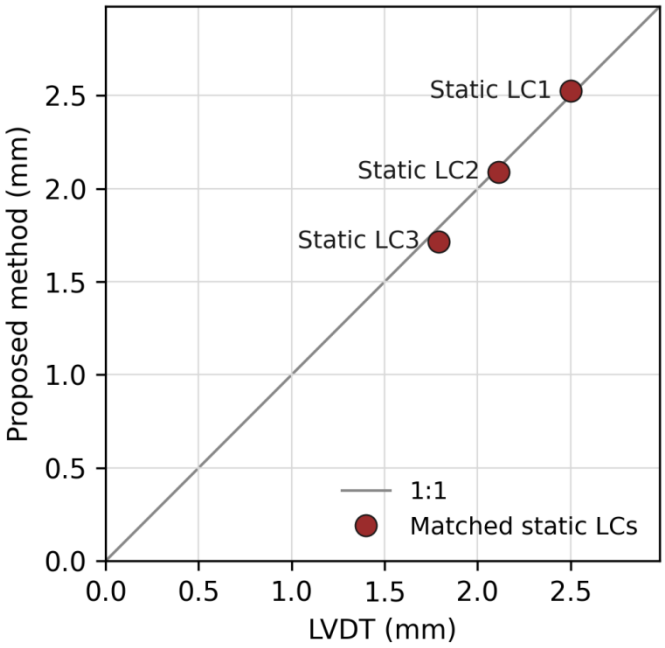


Fig. 20. Peak displacement comparison at G1 for the Static LC1–LC3 plateaus (n = 3 in Table 4).

Table 4. Quantitative comparison between LVDT measurements and offline displacement estimates at girder G1 (static n = 3: Static LC1–LC3 plateaus).

Dataset	MAE (mm)	RMSE (mm)	Peak |error| (mm)
Static matched peaks (n = 3)	0.040	0.046	0.073
Static aligned window (R = 0.847)	0.274	0.573	—
Dynamic aligned passage (R = 0.978)	0.055	0.083	0.472

4.4. Static Load Testing Analysis

The static load positions Static LC1–LC3 are shown in Fig. 21, and the estimated displacement time histories of G1 and G2 are shown in Fig. 22 with identical vertical scales.

In Static LC1, where the load is positioned near G1, the displacement of G1 is greater than that of G2. Conversely, at LC3, where the load is positioned near G2, the displacement of G2 exceeds that of G1. At the intermediate position LC2, both girders show response magnitudes between the two extreme cases. Table 5 summarizes the peak strains and displacements.

Fig. 23 presents the lateral load distribution, defined as the ratio of each girder response to the sum of both girder responses. The share carried by G1 decreases from Static LC1 to Static LC3 while that of G2 increases, for both strain and displacement.

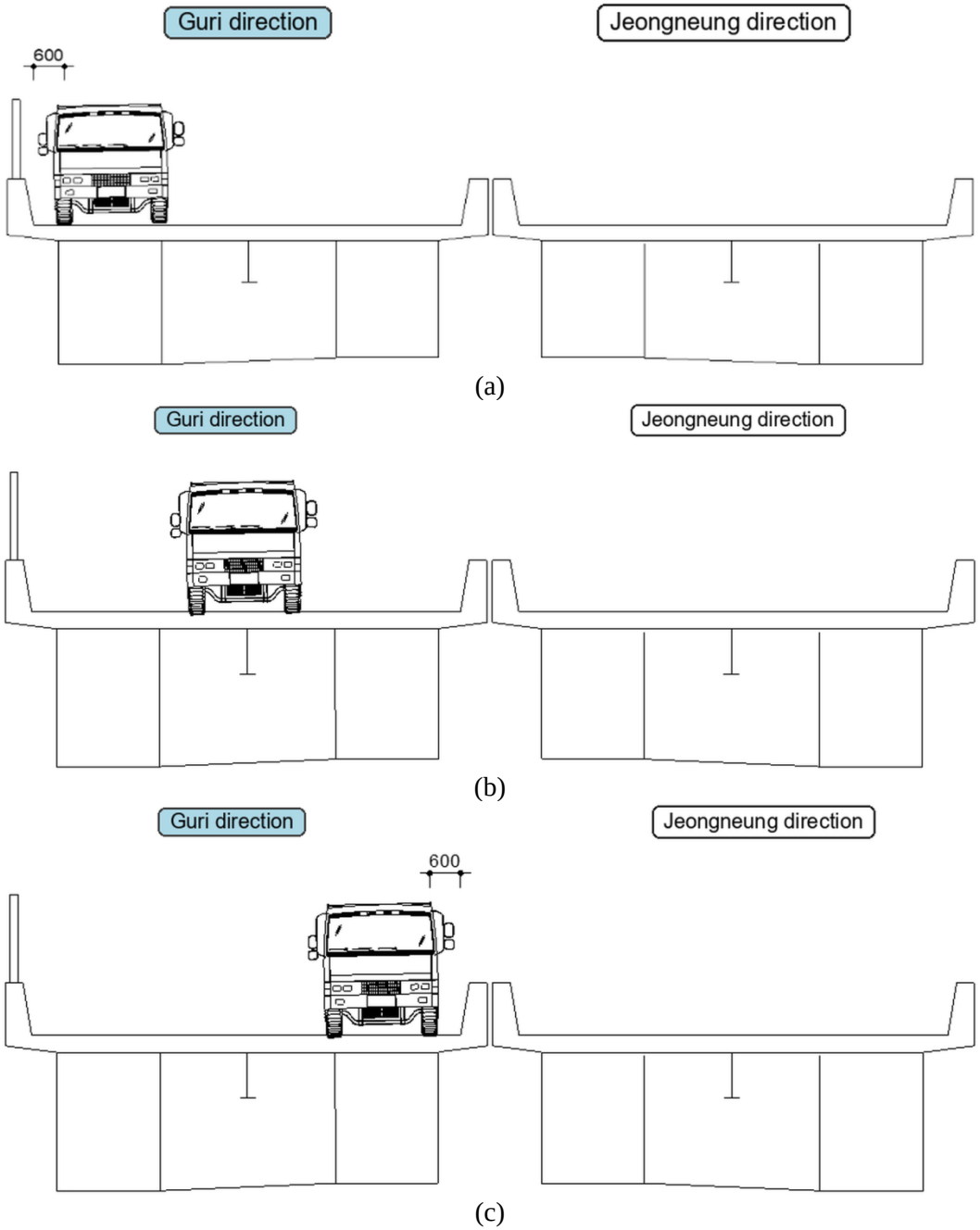


Fig. 21. Static load locations: (a) Static LC1; (b) Static LC2; (c) Static LC3.

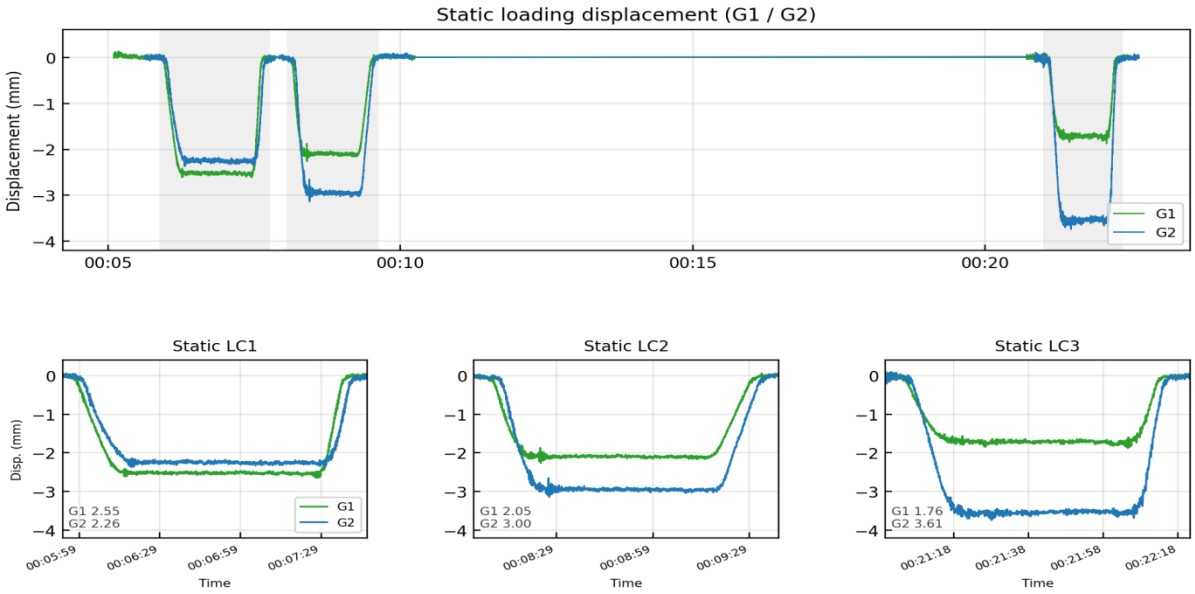


Fig. 22. Estimated static displacement histories for girders G1 and G2 (Static LC1–LC3).

Table 5. Static loading test results

Span			A–A section		
-		Unit	STATIC LC1	Static LC2	Static LC3
Strain	G1	$\mu\varepsilon$	47.80	38.77	29.63
	G2	$\mu\varepsilon$	31.45	42.76	51.89
Displacement	G1	mm	2.55	2.05	1.76
	G2	mm	2.26	3.00	3.61

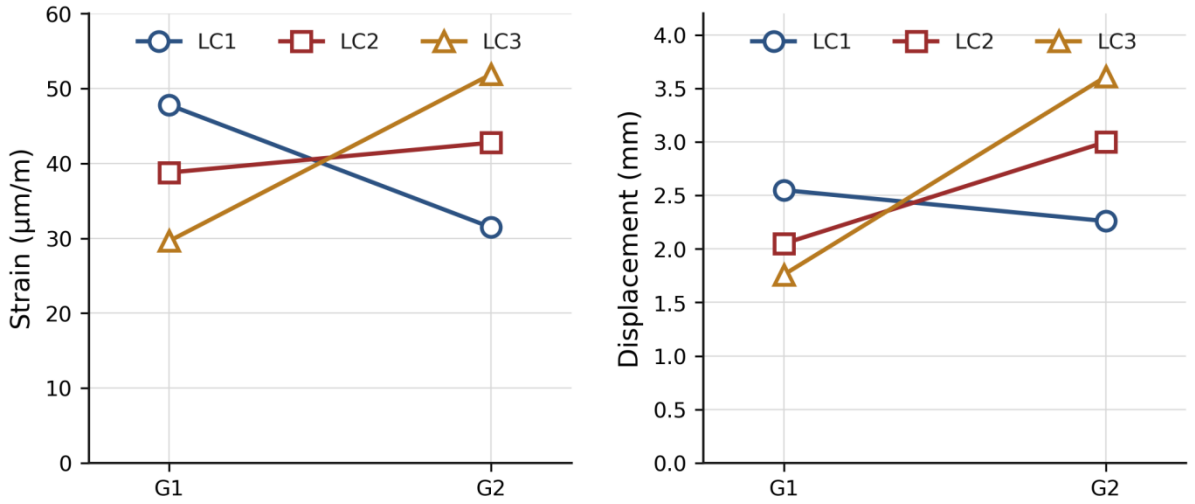


Fig. 23. Lateral load distribution analysis

The neutral axis (NA) of each girder section was then estimated as a supplementary indicator of global bending behavior. Under the assumption of a linear strain distribution between the top- and bottom-flange gauges, the NA height above the bottom flange is obtained as $y_{NA} = \varepsilon_b/(\varepsilon_b - \varepsilon_t)\cdot h$, where ε_b and ε_t are the measured bottom- and top-flange strains and h is the vertical gauge spacing (h = 2.4 m). The theoretical NA is 2.006 m above the bottom flange. The linear-strain assumption is approximate: localized wheel loading, shear lag, torsion or distortion of the box section, and gauge-positioning or bonding errors may produce departures from linearity. The NA estimates are therefore not interpreted as conclusive evidence of undamaged composite action.

The experimental NA values were within about 2–10% of the theoretical location for both girders (Table 6). The estimated NA was higher in the girder located under the load (G1 in Static LC1 and G2 in Static LC3, approximately 2.19–2.20 m) than in the less loaded girder (approximately 2.05–2.06 m). This difference may reflect local wheel-load effects and shear lag in the directly loaded girder. Neutral-axis estimates are reported for Static LC1 and LC3, which represent the extreme lateral load eccentricities; Static LC2 was omitted as the intermediate case.

Table 6. Neutral axis analysis result (bottom and top strains averaged over the settled plateau)

Girder	Load case	Bottom (με)	Top (με)	Experimental N.A. (m)	Theoretical N.A. (m)
G1	Static LC1	47.33	−4.40	2.196	2.006
	Static LC3	29.16	−5.05	2.046	
G2	Static LC1	30.54	−5.00	2.063	
	Static LC3	51.41	−4.85	2.193	

4.5. Dynamic Load Testing Analysis

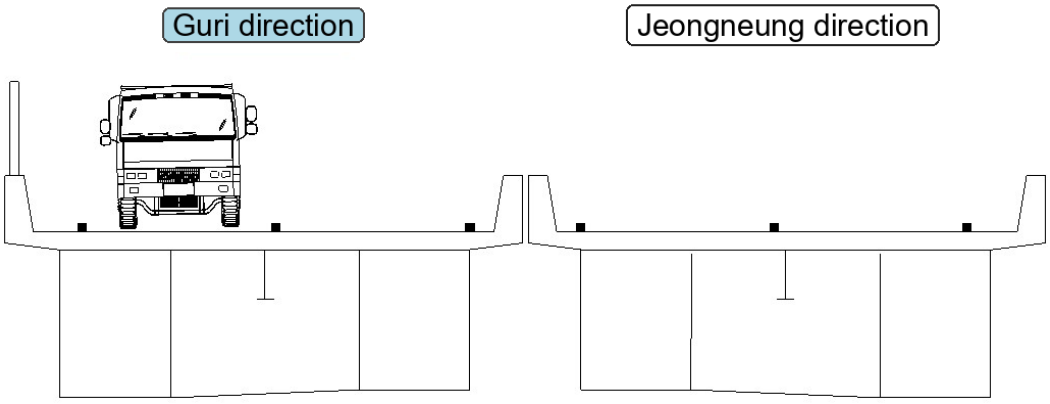


Fig. 24. Location of dynamic load.

Dynamic load testing (Fig. 24) was conducted to evaluate impact-related response indicators under truck speeds of 10–70 km/h. These quantities are reported as supplementary field indicators rather than as a definitive diagnosis of structural condition.

The dynamic amplification factor (DAF) represents the increase in structural response under moving loads relative to static loading and is related to the impact coefficient i as follows:

$$i = DAF - 1 \tag{11}$$

For each moving-load passage, the reconstructed displacement was first low-pass filtered at 5 Hz to obtain the dynamic response D_{dyn}; a subsequent 1 Hz low-pass filter then extracted the quasi-static component D_{sta} from the same passage. Peak values of D_{dyn} and D_{sta} were taken within each speed window. D_{sta} differs from the stationary static-test displacement and may vary among passes because the vehicle path differs. The impact coefficient was then evaluated as $i = (D_{dyn} - D_{sta})/D_{sta}$ as follows:

$$i_{measured} = \frac{\max(D_{dyn})}{\max(D_{sta})} - 1 \tag{12}$$

For comparison, the theoretical impact coefficient from the Korean Highway Bridge Design Code [53] is

$$i_{theory} = \frac{15}{40 + L} \tag{13}$$

where L is the span length between bearings (47.14 m), which gives a theoretical value of 0.172. The measured results are summarized in Table 7 and Fig. 25.

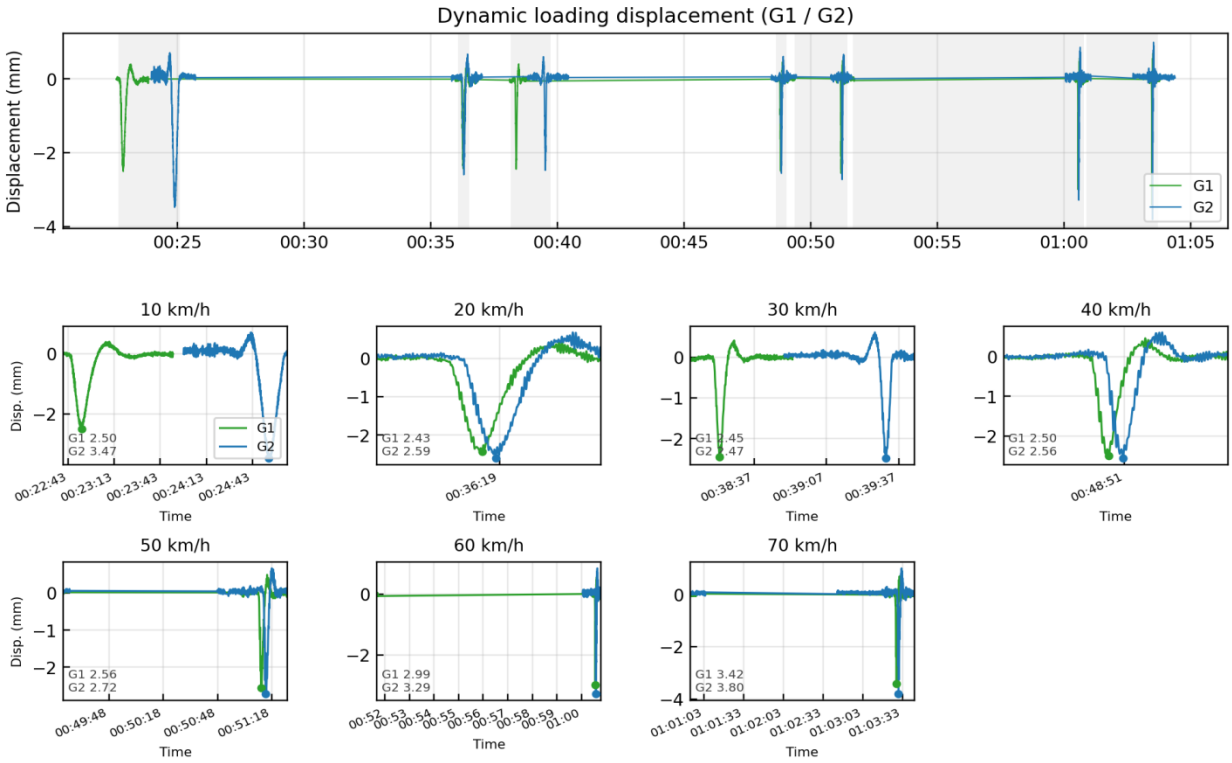


Fig. 25. Displacement analysis of dynamic loading tests.

At 10–50 km/h the measured impact coefficients remain below the theoretical value of 0.172 (maximum 0.068 for G1 and 0.083 for G2). They increase markedly between 50 and 60 km/h (G1: 0.068 → 0.227; G2: 0.083 → 0.323) and reach 0.408 (G1) and 0.542 (G2) at 70 km/h, exceeding the code reference at the higher speeds.

Table 7. Dynamic loading test results (D_{dyn}: 5 Hz peak; D_{sta}: 1 Hz peak; $i = (D_{dyn} - D_{sta})/D_{sta}$).

LOAD CASE	VALUE	G1	G2
Dynamic LC1 (10 km/h)	D_{dyn} (mm)	2.499	3.471
	D_{sta} (mm)	2.406	3.427
	i	0.039	0.013
Dynamic LC2 (20 km/h)	D_{dyn} (mm)	2.428	2.591
	D_{sta} (mm)	2.375	2.460
	i	0.022	0.053
Dynamic LC3 (30 km/h)	D_{dyn} (mm)	2.450	2.471
	D_{sta} (mm)	2.404	2.382
	i	0.019	0.037

Dynamic LC4 (40 km/h)	D_{dyn} (mm)	2.498	2.556
	D_{sta} (mm)	2.427	2.429
	i	0.029	0.052
Dynamic LC5 (50 km/h)	D_{dyn} (mm)	2.562	2.718
	D_{sta} (mm)	2.399	2.510
	i	0.068	0.083
Dynamic LC6 (60 km/h)	D_{dyn} (mm)	2.988	3.286
	D_{sta} (mm)	2.436	2.483
	i	0.227	0.323
Dynamic LC7 (70 km/h)	D_{dyn} (mm)	3.415	3.804
	D_{sta} (mm)	2.425	2.468
	i	0.408	0.542

4.6. Field Applicability of the Proposed Measurement System

The field results were compared with design-based references as follows.

First, the peak displacements estimated during static loading (Table 5) were smaller than the theoretical displacement obtained from the structural analysis in the load-test report of the 2023 precise safety diagnosis [52]. For the most critical case (G2, Static LC3), the maximum estimated displacement was 3.61 mm, while the corresponding analytical displacement was 4.429 mm, resulting in a response ratio (analytical to estimated) of 1.227. Because G2 had no reference LVDT, this value was not directly validated.

Second, the experimentally estimated neutral-axis locations agreed reasonably with the theoretical value under the linear-bending assumption discussed above.

Third, the impact coefficients from dynamic loading (Table 7) remain below the theoretical value (0.172) at 10–50 km/h and exceed it at 60–70 km/h.

Several limitations should be noted. Mode shapes were represented by an analytical sine approximation. Simultaneous multi-node triggering was demonstrated only in the laboratory at a command distance of about 2 m, and the timing accuracy of per-node alignment in the field was not quantified. Temperature was not measured, so thermal drift could not be compensated, although the short test duration limits its effect. The on-board acquisition chain was not cross-checked against a laboratory DAQ, and validation was performed at the system level against the co-located LVDT. Finally, the field validation is restricted to a steel box-girder span, and transfer to cracked concrete members requires separate verification because local cracking can weaken the strain–displacement relationship.

5. Conclusion

This study presented a portable multimetric sensing system for bridge load testing. The module integrates three-axis acceleration and four-channel strain acquisition with on-board storage and mobile-phone-based operation, which reduces cabling and removes the need for a base-station computer. Displacement is estimated offline from the strain and acceleration records after data download.

In laboratory tests, the acceleration noise levels were 0.47–1.55 mg across the three axes, the strain noise level was 0.69 με, and trigger offsets among simultaneously controlled nodes were within 0.05 s. In the field test on a steel box-girder span of the Bukbu Expressway, offline displacement estimates agreed with a co-located LVDT, with a maximum absolute peak error of 0.073 mm for the three matched static load cases and R = 0.978 (MAE = 0.055 mm) for an aligned dynamic passage. Neutral-axis positions agreed reasonably with the theoretical location under the stated assumptions; lateral load distribution is reported as observed girder shares (Fig. 23). The impact coefficients were below the code value at 10–50 km/h and larger at 60–70 km/h.

The results indicate that a single portable module can provide the strain, acceleration, and displacement responses required for load-carrying capacity evaluation without a cabled data logger, a base-station computer, or a fixed-reference displacement transducer. Because each node is checked and started on site with a mobile phone, its signals can be inspected before loading begins. Future work will extend the validation to other bridge types, including concrete bridges, and add temperature channels for longer measurements.

References

1. Brighenti, F., et al., *Bridge management systems: A review on current practice in a digitizing world.* Engineering Structures, 2024. **321**: p. 118971.
2. Frangopol, D.M., J.S. Kong, and E.S. Gharaibeh, *Reliability-based life-cycle management of highway bridges.* Journal of Computing in Civil Engineering, 2001. **15**(1): p. 27–34.
3. Biondini, F. and D.M. Frangopol, *Life-cycle performance of deteriorating structural systems under uncertainty.* Journal of Structural Engineering, 2016. **142**(9): p. F4016001.
4. Alampalli, S., et al., *Bridge load testing: State-of-the-practice.* Journal of Bridge Engineering, 2021. **26**(3): p. 03120002.
5. Wang, N., et al., *Bridge rating using system reliability assessment. I: Assessment and verification by load testing.* Journal of Bridge Engineering, 2011. **16**(6): p. 854–862.
6. Douglas, B.M. and W.H. Reid, *Dynamic tests and system identification of bridges.* Journal of the Structural Division, 1982. **108**(10): p. 2295–2312.
7. Turner, D.S. and J.A. Richardson, *Bridge management system data needs and data collection.* Transportation Research Circular, 1994. **423**: p. 5–15.
8. Alokita, S., et al., *Recent advances and trends in structural health monitoring,* in Structural Health Monitoring of Biocomposites, Fibre-Reinforced Composites and Hybrid Composites, M. Jawaid, M. Thariq, and N. Saba, Editors. 2019, Woodhead Publishing (Elsevier): Duxford. p. 53–73.

9. Bhatta, S. and J. Dang, *Use of IoT for structural health monitoring of civil engineering structures: a state-of-the-art review.* Urban Lifeline, 2024. **2**(1): p. 17.
10. Elsisi, A., A. Zamrawi, and S. Emad, *A Comprehensive Review of Structural Health Monitoring for Steel Bridges: Technologies, Data Analytics, and Future Directions.* Applied Sciences, 2025. **15**(22): p. 12090.
11. Sonbul, O.S. and M. Rashid, *Towards the structural health monitoring of bridges using wireless sensor networks: A systematic study.* Sensors, 2023. **23**(20): p. 8468.
12. Mardanshahi, A., et al., *Sensing techniques for structural health monitoring: A state-of-the-art review on performance criteria and new-generation technologies.* Sensors, 2025. **25**(5): p. 1424.
13. Sony, S., S. Laventure, and A. Sadhu, *A literature review of next-generation smart sensing technology in structural health monitoring.* Structural Control and Health Monitoring, 2019. **26**(3): p. e2321.
14. Yang, Y., et al., *Research progress on calibration of bridge structural health monitoring sensing system.* Advances in Bridge Engineering, 2024. **5**(1): p. 32.
15. Hu, X., G. Olgun, and R.H. Assaad, *An intelligent BIM-enabled digital twin framework for real-time structural health monitoring using wireless IoT sensing, digital signal processing, and structural analysis.* Expert Systems with Applications, 2024. **252**: p. 124204.
16. Tan, Z., et al., *Digital twin-based cyber-physical system for intelligent monitoring and predictive operation of long-span high-speed railway arch bridges.* Structures, 2025. **82**: p. 110609.
17. Valinejadshoubi, M., et al., *Digital Twin Construction in Practice: A Case Study of Closed-Loop Production Control Integrating BIM, GIS, and IoT Sensors.* Journal of Construction Engineering and Management, 2025. **151**(11): p. 05025014.
18. Gao, Y., et al., *AIoT-informed digital twin communication for bridge maintenance.* Automation in Construction, 2023. **150**: p. 104835.
19. Khayam, S.U., et al., *Monitoring Precast Structures During Transportation Using A Portable Sensing System.* Automation in Construction, 2023. **145**: p. 104639.
20. Lander, P., N. Fahed, and Y. Wang, *Martlet wireless sensing system for full scale bridge weigh-in-motion.* Proc. SPIE 12046, Sensors and Smart Structures Technologies for Civil, Mechanical, and Aerospace Systems 2022, 1204605 (2022).
21. Park, J.-Y., et al., *Development of low-power IoT sensor and cloud-based data fusion displacement estimation method for ambient bridge monitoring.* Journal of the Computational Structural Engineering Institute of Korea, 2021. **34**(5): p. 301–308.
22. Park, J., J. Shin, and J. Park, *Development of IoT sensor and cloud-based server for cloud-based bridge long-term monitoring.* arXiv preprint arXiv:2209.12186, 2022.
23. Spencer Jr, B., et al., *Next generation wireless smart sensors toward sustainable civil infrastructure.* Procedia Engineering, 2017. **171**: p. 5–13.
24. Zhang, M., et al., *Fully automated and robust cable tension estimation of wireless sensor networks system.* Sensors, 2021. **21**(21): p. 7229.
25. Chae, M., et al., *Development of a wireless sensor network system for suspension bridge health monitoring.* Automation in Construction, 2012. **21**: p. 237–252.
26. He, Z., et al., *Integrated structural health monitoring in bridge engineering.* Automation in Construction, 2022. **136**: p. 104168.
27. Yu, X., et al., *Recent advances in wireless sensor networks for structural health monitoring of civil infrastructure.* Journal of Infrastructure Intelligence and Resilience, 2024. **3**(1): p. 100066.
28. Ma, Z., J. Choi, and H. Sohn, *Structural displacement sensing techniques for civil infrastructure: A review.* Journal of Infrastructure Intelligence and Resilience, 2023. **2**(3): p. 100041.
29. Nhung, N.T.C., et al., *Development and application of linear variable differential transformer (LVDT) sensors for the structural health monitoring of an urban railway bridge in Vietnam.* Engineering, Technology & Applied Science Research, 2023. **13**(5): p. 11622–11627.

30. An, X., et al., *GNSS integrated displacement and attitude determination for structural health monitoring of long-span bridges.* Satellite Navigation, 2025. **6**(1): p. 19.
31. Ma, Z., J. Choi, and H. Sohn, *Continuous bridge displacement estimation using millimeter-wave radar, strain gauge and accelerometer.* Mechanical Systems and Signal Processing, 2023. **197**: p. 110408.
32. Ma, Z., et al., *Bridge displacement estimation by fusing accelerometer and strain gauge measurements.* Structural Control and Health Monitoring, 2021. **28**(6): p. e2733.
33. Qu, X., X. Ding, and Y.-L. Xu, *Simultaneous monitoring of displacement and rotation of a long-span bridge based on innovative integration of GNSS and accelerometer measurements.* Engineering Structures, 2025. **338**: p. 120518.
34. Sarwar, M.Z. and J.-W. Park, *Bridge displacement estimation using a co-located acceleration and strain.* Sensors, 2020. **20**(4): p. 1109.
35. Won, J., et al., *Development of a reference-free indirect bridge displacement sensing system.* Sensors, 2021. **21**(16): p. 5647.
36. Park, J.-W., S.-H. Sim, and H.-J. Jung, *Displacement estimation using multimetric data fusion.* IEEE/ASME Transactions on Mechatronics, 2013. **18**(6): p. 1675–1682.
37. Barasa, W., et al., *Monitoring displacement, strain, and acceleration of a steel railway bridge.* Ain Shams Engineering Journal, 2023. **14**(11): p. 102521.
38. Khan, S., et al., *SSVM: An ultra-low-power strain sensing and visualization module for long-term structural health monitoring.* Sensors, 2021. **21**(6): p. 2211.
39. Lawal, O., et al., *Development and validation of a framework for smart wireless strain and acceleration sensing.* Sensors, 2022. **22**(5): p. 1998.
40. López-Castro, B., et al., *A systematic review of structural health monitoring systems to strengthen post-earthquake assessment procedures.* Sensors, 2022. **22**(23): p. 9206.
41. PJRC. *Teensy 4.1 Development Board.* PJRC Store 2024 [cited 2026-01-09]; Available from: https://www.pjrc.com/store/teensy41.html.
42. Texas Instruments, *ADS131E08 Data Sheet.* 2017.
43. Taher, S.A., et al., *Structural health monitoring of fatigue cracks for steel bridges with wireless large-area strain sensors.* Sensors, 2022. **22**(14): p. 5076.
44. Analog Devices, Inc., *ADXL354/ADXL355 Low Noise, Low Drift, Low Power, 3-Axis MEMS Accelerometer*. 2024.
45. Analog Devices, Inc., *DS3231 Extremely Accurate I²C-Integrated RTC/TCXO/Crystal Data Sheet.* 2015.
46. Firmtech Co., Ltd., *FB755AS Bluetooth Embedded Module.* 2025 [cited 2026-01-09]; Available from: https://firmtech9.cafe24.com/product/fb755as/30/.
47. Texas Instruments, *TPS752xx-EP w/Reset TPS754xx-EP w/Power Good Fast Trans Response Voltage Regulators Datasheet.* 2003.
48. Micro-Measurements, Optimizing Strain Gage Excitation Levels, Tech Note TN-502 (Document No. 11052). 2010, Vishay Precision Group.
49. Lee, H.S., Y.H. Hong, and H.W. Park, Design of an FIR filter for the displacement reconstruction using measured acceleration in low-frequency dominant structures. International Journal for Numerical Methods in Engineering, 2010. 82: p. 403–434.
50. Tokyo Measuring Instruments Laboratory Co., Ltd., *TML F Series Foil Strain Gauges Product List.* 2025.
51. Seoul Facilities Corporation, *Seoul Urban Expressway Traffic Volume Statistics (Bukbu Expressway).* 2025: Seoul, Republic of Korea.
52. Seoul Facilities Corporation, *Detailed Safety Inspection and Condition Assessment Report for the Bukbu Urban Expressway Overpass.* 2024: Seoul, Republic of Korea.
53. Ministry of Land, Infrastructure and Transport, Republic of Korea, *Korean Design Standard (KDS) 24 10 10: Bridge Design — General Provisions.* 2021: Seoul, Republic of Korea.

Acknowledgments

This research was funded by the Korea Agency for Infrastructure Technology Advancement (KAIA) grant funded by the Ministry of Land, Infrastructure, and Transport (RS-2022-00142239).